PREDICTION OF FORT WORTH TORNADIC THUNDERSTORMS USING 3DVAR AND CLOUD ANALYSIS WITH WSR-88D LEVEL-II DATA

Ming Hu[1,2], Ming Xue[*1,2], Keith Brewster[1] and Jidong Gao[1]
[1]Center for Analysis and Prediction of Storms
[2]School of Meteorology
University of Oklahoma, Norman, OK 73019

1. INTRODUCTION

The development of high-resolution nonhydrostatic models and the rapid increase of computer power are making the explicit prediction of thunderstorms a reality (Droegemeier 1990; Lilly 1990; Droegemeier 1997; Xue *et al.* 2003, X03 hereafter). Data assimilation plays an important role in providing an accurate initial condition for the model forecast. The operational US WSR-88D Doppler radar network (Crum and Alberty 1993) is a key source of data for initializing storm-scale numerical weather prediction (NWP) models as it the only operational platform capable of providing observations of spatial and temporal resolutions sufficient for resolving convective storms.

The analysis of radar data to arrive at a complete set of initial conditions for a NWP model is challenging, because radars only observe a very limited set of parameters, the most important being the radial velocity and reflectivity. Their spatial coverage is often incomplete. To determine atmospheric state variables that are not directly observed, certain retrieval or assimilation techniques have to be used.

Four-dimensional variational (4DVAR) data assimilation, which obtains a full set of model initial conditions that provides the best fit between the model solution and radar observations within a time (assimilation) window, is considered ideal for this purpose. Some encouraging 4DVAR results with both simulated and real radar data have been obtained by, for example, Sun et al. (1991; 1997; 1998). On the other hand, the complexity of developing and maintaining the adjoint code needed by a 4DVAR system and the high computational cost of 4DVAR technique for high-resolution applications are limiting its use in research and operation. Another relatively new technique is the ensemble Kalman filter (EnKF) method, which has been shown recently to produce single-Doppler radar analyses of thunderstorms that are of similar quality as the 4DVAR analysis (Snyder and Zhang 2003; Tong and Xue 2004; Zhang *et al.* 2004). While also expensive because of the need for running an analysis and forecast ensemble of significant sizes, EnKF method enjoys the simplicity in implementation and is much more flexible.

Other simpler, yet faster, methods exist that attempt to retrieve unobserved variables from the radar data. The retrieved state variables can then be analyzed into the model initial conditions. The wind retrieval methods include the so-called simple adjoint method (Qiu and Xu 1992; Qiu and Xu 1994; Xu *et al.* 1994; Gao *et al.* 2001) and two-scalar method of Shapiro et al. (1995), among others. The former employs a simple prognostic equation and its adjoint to determine the advective winds that produce the best fit between the predicted and observed radial velocity and/or reflectivity. The latter method is based on the conservation of two scale quantities and is demonstrated by Weygandt et al. (2002a). Additionally, the retrieved three-dimensional wind fields at more than one time level can be used to retrieve additionally thermodynamic fields (Gal-Chen 1978). The retrieved fields can then be combined via an analysis procedure, as is done in Weygandt et al. (2002b). Such multi-step procedures have the advantages of being able to make use of multiple radar volume scans in an inexpensive way, but the involvement of multiple steps and the use of retrieved instead of direct observations make the optimality of analysis difficult to impose.

Another alternative is to analyze the radial velocity data directly via a three-dimensional variational (3DVAR) analysis procedure. Certain dynamic or equation constraints can be built into the 3DVAR cost function with relative ease. Such a system has been developed within the ARPS model (Xue *et al.* 1995; 2000; 2001) framework and documented in Gao et al. (2002; 2004). It is used in this study to analyze radial velocity and

* Corresponding Author Address: Dr. Ming Xue, School of Meteorology, University of Oklahoma, 100 East Boyd, Norman, OK 73019.
E-mail: mxue@ou.edu.

other conventional observations. The 3DVAR method is theoretically less optimal than 4DVAR but computationally much faster. We assimilate multiple radar volume scans by performing intermittent assimilation cycles.

The inclusion of reflectivity data into a 3DVAR system for the purpose of thermodynamic and microphysical retrievals and analysis is not straightforward, because the problem is underdetermined. Semi-empirical rules can be used to aid the analysis of these fields. This is done within the ADAS (ARPS Data Analysis System, Brewster 1996) cloud analysis procedure, which has evolved from that used in the Local Analysis and Prediction System (LAPS, Albers *et al.* 1996) cloud analysis with previous modifications documented by Zhang et al (1998) and Zhang (1999) The cloud analysis procedure has been included in the ARPS 3DVAR analysis systems. In X03 the Bratseth-based (Bratseth 1986) ADAS analysis scheme combined with the cloud analysis is applied to the March 28, 2000 Fort Worth tornado case. Level-III (NIDS) reflectivity data are assimilated at 15 minute intervals in that work. While the results are encouraging, significant discrepancies in the predicted storms are noted in the paper. In this work, as an attempt to improve the assimilation and forecast, we replace the ADAS analysis scheme with the ARPS 3DVAR system and assimilate the radial velocity data directly, with the inclusion of a 3D mass continuation equation as a constraint to the wind fields. We employ an improved version of the cloud analysis that includes a different scheme for temperature adjustment in the cloud regions and modifications to other parts of the procedure. In addition, we use the more accurate full-volume Level II instead of the Level III data that are of reduced accuracy and only include the 4 lowest tilts of data.

We firstly focus on the use of radial velocity data via the 3DVAR procedure. We then examine the impact of improved cloud analysis procedure and each modification individually. The organization is as follows. In Section 2, we briefly introduce the ARPS 3DVAR system, including the important aspects of radial velocity analysis and the mass continuity constraint. In Section 3, the previous cloud analysis scheme and the modifications to it are described in detail. In Section 4, we describe the tornado outbreak case and the design of experiments for determining the impact of radial velocity data, the improved cloud analysis and each modification. The detailed results are presented in Section 5. A summary is provided in Section 6.

2. THE ARPS 3DVAR SYSTEM

a. The basic scheme

Following Gao et al. (2004), the standard cost function of 3DVAR can be written as

$$J(\mathbf{x}) = \frac{1}{2}\left(\mathbf{x}-\mathbf{x}^b\right)^T \mathbf{B}^{-1}\left(\mathbf{x}-\mathbf{x}^b\right) + \frac{1}{2}\left[H(\mathbf{x})-\mathbf{y}^o\right]^T \mathbf{R}^{-1}\left[H(\mathbf{x})-\mathbf{y}^o\right] + J_c, \quad (1)$$

where the first term on the right hand side measures the departure of the analysis vector, $\boldsymbol{x}$, from the background, $\boldsymbol{x}^b$, weighted by the inverse of the background error covariance matrix **B**. In the current ARPS 3DVAR system, the analysis vector $\boldsymbol{x}$ contains the three wind components (u, v, and w), potential temperature (θ), pressure (p) and water vapor mixing ratio (q_v). The second, observation term, measures the departure of the analysis from the observation vector $\mathbf{y}^o$. The analysis is projected to the observation space by the forward operator, H, and the observation term is weighted by the inverse of observation error covariance matrix **R**. J_c represents dynamic or equation constraints.

Transforming control variables from **x** to **v**, according to $\sqrt{\mathbf{B}}\mathbf{v} = \left(\mathbf{x}-\mathbf{x}^b\right)$, the standard cost function is changed into incremental form:

$$J_{inc} = \frac{1}{2}\mathbf{v}^T\mathbf{v} + \frac{1}{2}\left(\mathbf{H}\sqrt{\mathbf{B}}\mathbf{v}-\mathbf{d}\right)^T \mathbf{R}^{-1}\left(\mathbf{H}\sqrt{\mathbf{B}}\mathbf{v}-\mathbf{d}\right) + J_c, \quad (2)$$

where **H** is the linearized version of H and $\mathbf{d} \equiv \mathbf{y}^o - H\left(\mathbf{x}^b\right)$. In the current system, the cross-correlations between variables are not included in the background error covariances. The background error correlations for single control variables are modeled by a recursive spatial filter. The observation errors are assumed to be uncorrelated, that is, **R** is a diagonal matrix, and its diagonal elements are specified according to the estimated observation errors.

Considering different data types represent very different spatial scales, ARPS 3DVAR allows the use of multiple analysis passes, with each one using different data types and filter scales.

b. Radar radial velocity

For the radial velocity observations, the forward operator, or H in Eq.(1), that projects the velocity into the radial direction, is

$$V_r = \frac{(X - X_o)u + (Y - Y_o)u + (Z - Z_o)w}{r}, \qquad (3)$$

where u, v and w are the wind components in Cartesian coordinates (X, Y, Z); and (X_o, Y_o, Z_o) are the coordinates of radar; r is the distance from radar location to the observation points of radial velocity. In ARPS 3DVAR, the observed radial velocity data are first interpolated to analysis grid points through preprocessing and therefore no further spatial interpolation is needed in this forward operator. The preprocessing program also includes quality control (velocity dealiasing, clutter removal, etc.) and takes into account the spherical geometry of the earth.

c. Mass continuity constraint

In the ARPS 3DVAR, the following weak anelastic mass continuity constraint is imposed on the analyzed wind field:

$$J_c = \frac{1}{2}\lambda_c^2 D^2 \qquad (4)$$

where λ_c is a weighting coefficient that controls the relative importance of this penalty term in the cost function. *D* has the form of

$$D = \alpha\left(\frac{\partial \bar{\rho}u}{\partial x} + \frac{\partial \bar{\rho}v}{\partial y}\right) + \beta\frac{\partial \bar{\rho}w}{\partial z} \qquad (5)$$

where $\bar{\rho}$ is the mean air density at given height levels, α and β are coefficients that are unity when the regular three-dimensional mass continuity or divergence constraint is used. Different choices of their values will be tested in a set of analysis experiments to be presented later. When α = β =1, the mass continuity constraint acts to minimize the three-dimensional divergence and in the analysis process couples the three wind components together. Gao et al (2004) found that the 3D formulation is effective in producing reasonable analyses of vertical velocity which is little observed by the two Doppler radars in their case and for their ratio of horizontal to vertical grid spacing (close to unity).

When used in a finite difference form, we found that the third term on the right hand side of Eq.(5), i.e., the vertical mass divergence term, dominates the adjustment of J_c in cases where the horizontal grid interval is much larger than the vertical one. For example, when $\Delta x = \Delta y = \gamma\Delta z$, Eq. (5) is discretized as

$$D = \frac{\Delta(\bar{\rho}u) + \Delta(\bar{\rho}v)}{\gamma\Delta z} + \frac{\Delta(\bar{\rho}w)}{\Delta z}. \qquad (6)$$

When the value of γ (defined as the grid aspect ratio) is large, say over 100, as is the case at the levels near the ground in our experiments, a small adjustment in the vertical velocity can offset a large change in the horizontal wind divergence. The result is that little change due to this constraint is made by the minimization to the horizontal wind components. One possibility is to use different values of α and β, or even set β to zero to alleviate this artifact of discretization.

To illustrate the above points, we conducted three experiments, in which a single radial velocity observation (taken to be along the *x* direction) is analyzed, using (a) no mass continuity constraint (α=β=0), (b) using a 2D divergence constraint (α=1, β=0), and (c) using a fully 3D divergence constraint (α=β=1). Further, to isolate the effect of mass continuity constraint, we do not include the recursive filter in these tests. The results of these experiments are plotted in Fig. 1. It can be seen that without mass continuity constraint, no *y* component (or cross-beam component) of velocity is produced by the analysis, i.e., the analysis is purely uni-variant (Fig. 1a). No vertical velocity is created either in this case (not shown). When the 2D mass divergence is used, a single radial velocity observation induces a horizontal flow pattern that is nearly non-divergent (Fig. 1b) while no vertical velocity develops (not shown). When a complete 3D divergence appears in J_c, most of the wind adjustment occurs in vertical velocity, as is shown by Fig. 1c, while little adjustment occurs to the *y* (horizontal cross-beam) component (Fig. 1d), a result very similar to the unconstrained case. The correct solution should be somewhere between cases two and three. In addition, when the recursive filter is applied, the analysis will appear smoother and the analysis increment will spread over a larger area.

One of the goals of including mass continuity constraint in the radial velocity analysis is to induce wind information perpendicular to radar beams. From above analysis, the three-dimensional mass continuity constraint cannot achieve the desired effect in the horizontal flow when the grid aspect ratio is large, which is true for our case. For this reason, the two-dimensional mass continuity constraint is used in the control and related experiments and an additional set of experiments is performed to examine the impact of different formulations of the mass continuity constraint on the analysis and forecast. We note here because the equation is used as a weak constraint, it is not strictly satisfied, which gives the analysis some flexibility in determining the

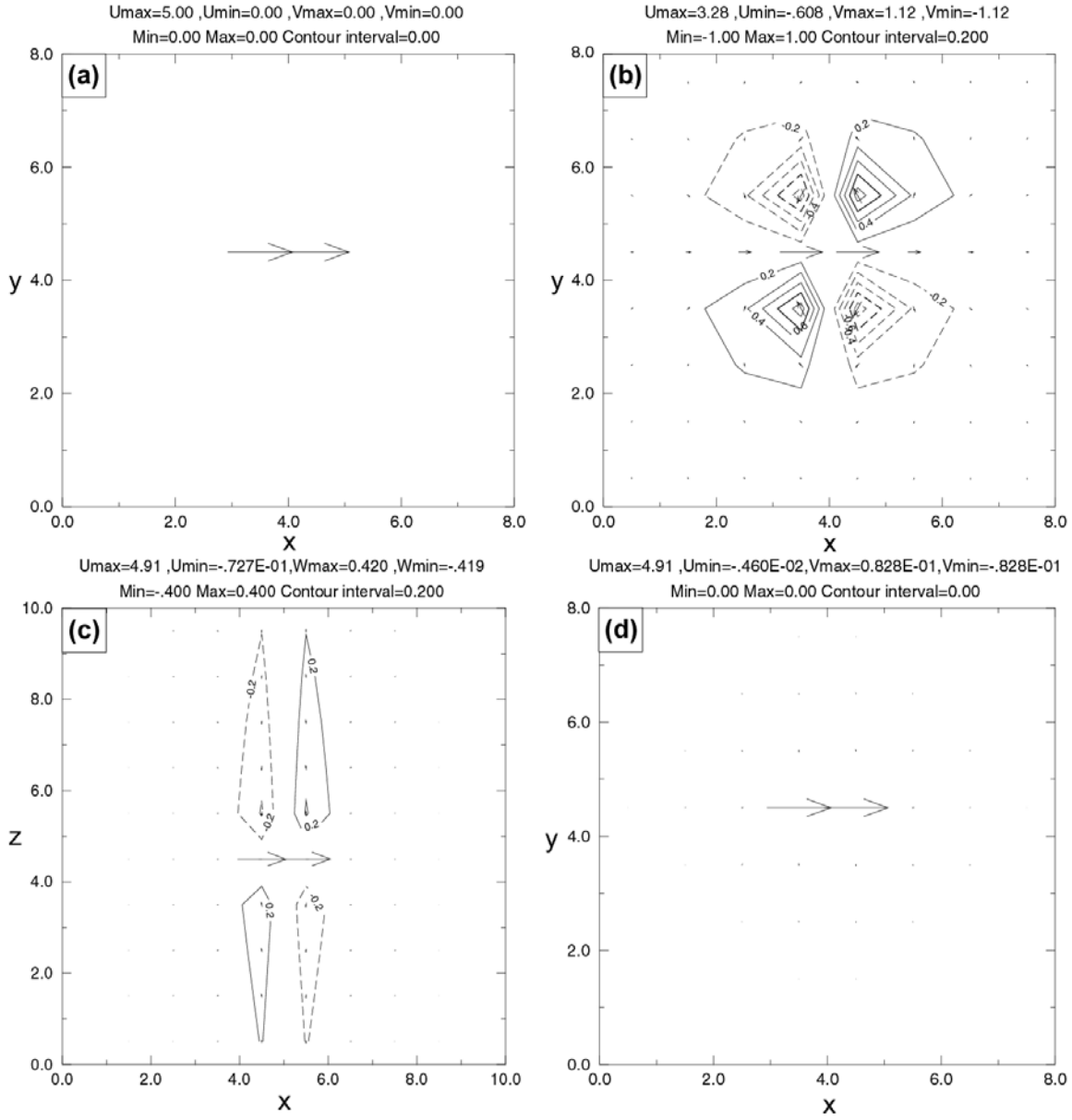

Fig. 1. Results of 3DVAR analyzing a single radial wind measurement (pointing in positive *x* direction) with different mass continuity constraints. The background wind is zero. a) wind analysis without applying mass continuity constraint, b) the x-y cross-section of u-v wind analyzed with a 2D (horizontal) mass continuity constraint, c) x-z cross-section of u-w wind after applying a 3D mass continuity constraint, and d) as b) but with a 3D continuity constraint.

amount of adjustment to different wind components.

3. CLOUD ANALYSIS

The cloud analysis procedure is a component separate from the basic analysis procedure in both ARPS 3DVAR and the ADAS analysis systems. It is a customization of the algorithms used by the Forecast Systems Lab LAPS with several refinements and enhancements. It incorporates cloud reports from surface observing of Global Observing System (GOS) of World Meteorological Organization (WMO), standard Aviation Routine Weather Reports (METARs), satellite infrared and visible imagery data, and radar reflectivity data to construct three-dimensional cloud and precipitate fields. The products of the analysis package include three-dimensional cloud cover,

cloud liquid and ice mixing ratios, cloud and precipitate types, icing severity index, and rain, snow and hail mixing ratios. Cloud base, top and cloud ceiling fields are also derived. A latent heat adjustment to temperature based on added adiabatic liquid water content is applied, so that the in-cloud temperature is reasonably consistent with the water fields. More details on the package can be found in the references quoted in Section 1.

The above version of cloud analysis was used by the experiments in X03. In most experiments presented here, the improved cloud analysis procedure is used to assimilate reflectivity data into the model initial field. In this section, we will introduce these modifications to cloud analysis scheme with examples from corresponding analysis experiments. For the convenience of introduction, we call the cloud analysis method used in X03 the old scheme and the modified cloud analysis method used in this paper the new scheme.

a. The analysis of precipitation species

1) Equations for defining precipitate mixing ratio from reflectivity:

To emphasize the impact of radar data, satellite data and surface cloud observations are not used in the cloud analysis procedure in this paper. The reflectivity equations used by the new analysis procedure for the retrieval of three dimensional precipitation species is based on those of Smith, Myers and Orville (1975) with slight differences. The actual formulae used are described in Tong and Xue (2004). Similar formulae are also used by Ferrier (1994). In this paper, retrieval of precipitation species is the process that derives precipitation species from observed reflectivity and background environment via radar reflectivity equations but no background precipitation species are used in the process. The reflectivity is divided into three components due to contributions from rain, snow, and hail respectively. Each reflectivity component can be calculated by a function including the mixing ratio of corresponding hydrometer and environment variables. Based on precipitation types identified according to reflectivity and environment variables from the output of the basic analysis scheme such as 3DVAR, the equations for the reflectivity components are used to determine the mixing ratios of rainwater, snow and hail. We refer to this precipitation species retrieval scheme the SMO scheme.

In the old cloud analysis procedure, the rainwater mixing ratio is retrieved using Kessler reflectivity equation (Kessler 1969), and snow and hail are retrieved using Rogers and Yau (1989) reflectivity formula. Hereafter we refer to this hydrometer retrieval scheme as the KRY scheme.

The SMO scheme considers more detailed cloud physics processes and should yield hydrometer fields that are more accurate than KRY scheme does.

2) The reflectivity used in the retrieval equations

In the region of the model domain covered by the radar scan volume, the new scheme classifies grid points into clear, precipitation-filled, and missing observation categories according to a threshold of reflectivity, which is an adjustable parameter and set to 10 dBZ in all experiments in this paper. A grid point with observed reflectivity greater than or equal to the threshold is treated as precipitation-filled and its precipitation species will be retrieved by the SMO scheme from the observed reflectivity. Any point with observed reflectivity that ranges from –20 dBZ to the threshold is treated as clear and its precipitation species are set to zero. The point that does not belong to above two categories falls into the missing observation category, and background values (usually from previous forecast) are used for its precipitation species. In the KRY scheme, the threshold is fixed at 0 dBZ. The points with reflectivity greater than 0 dBZ are considered to be precipitation-filled and all other points are treated as precipitation-free.

For the area that is outside the observed range of the radar, both schemes use background values for the precipitating hydrometeors. For the point below the first radar elevation scan, the old scheme sets the precipitation species to zero while new scheme uses the background value that is further adjusted to disallow the sum of rain, snow and hail mixing ratios to exceed the maximum value of the same in the column above.

Figure 2 shows the retrieved precipitation species by old scheme (left column) and new scheme (right column) from the same radar observation and the environmental analysis. The old scheme gives much more hail and rain but less snow than new scheme. These figures illustrate that the old scheme is designed for warm rain that has not much vertical extent. In the rain field determined by the new scheme, the large values under the first radar tilt come from the background

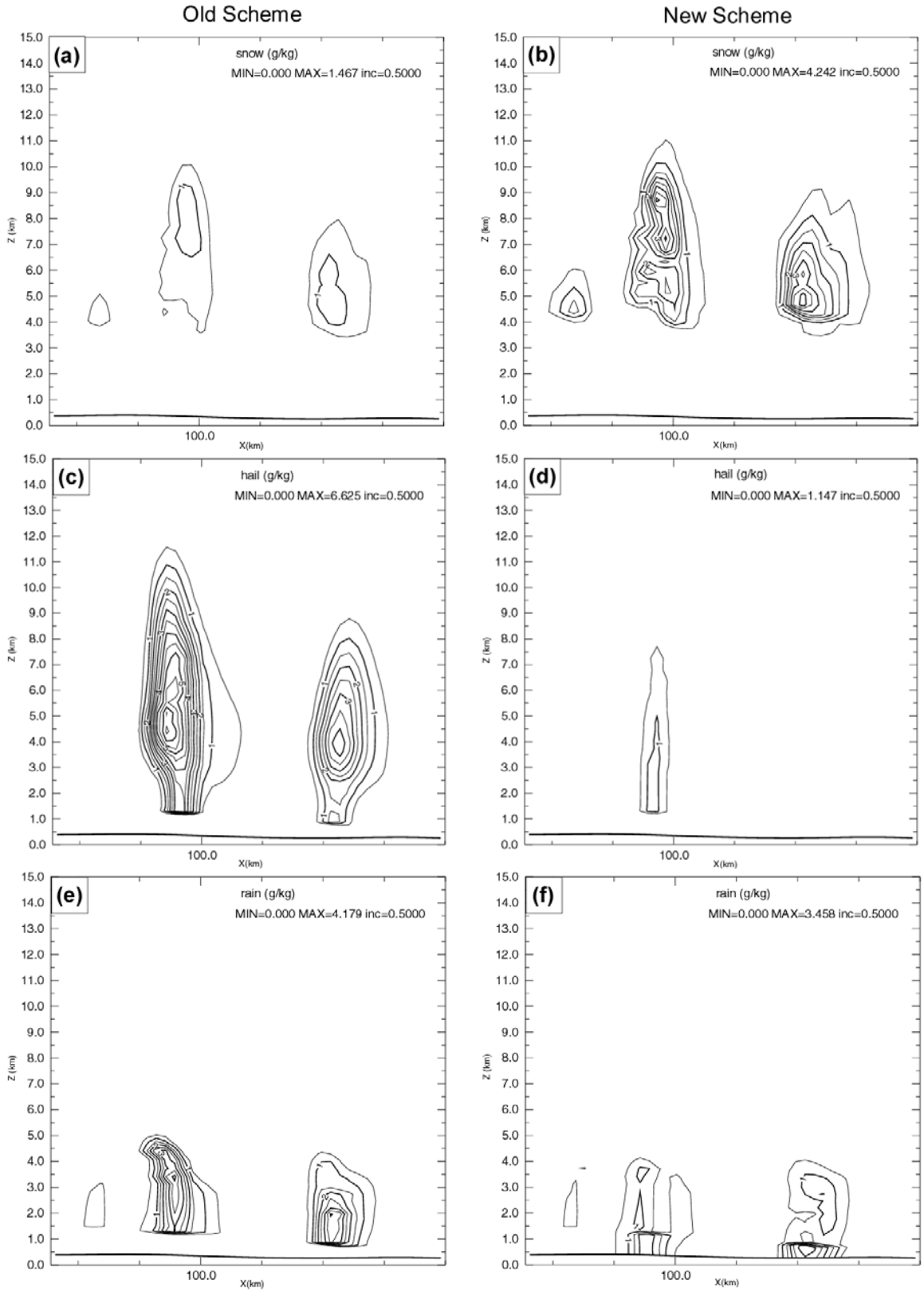

Fig. 2. Cross section of retrieved quantities of snow, hail, and rain fields by the old (KRY) scheme and the new (SMO) scheme from same radar observation and environment.

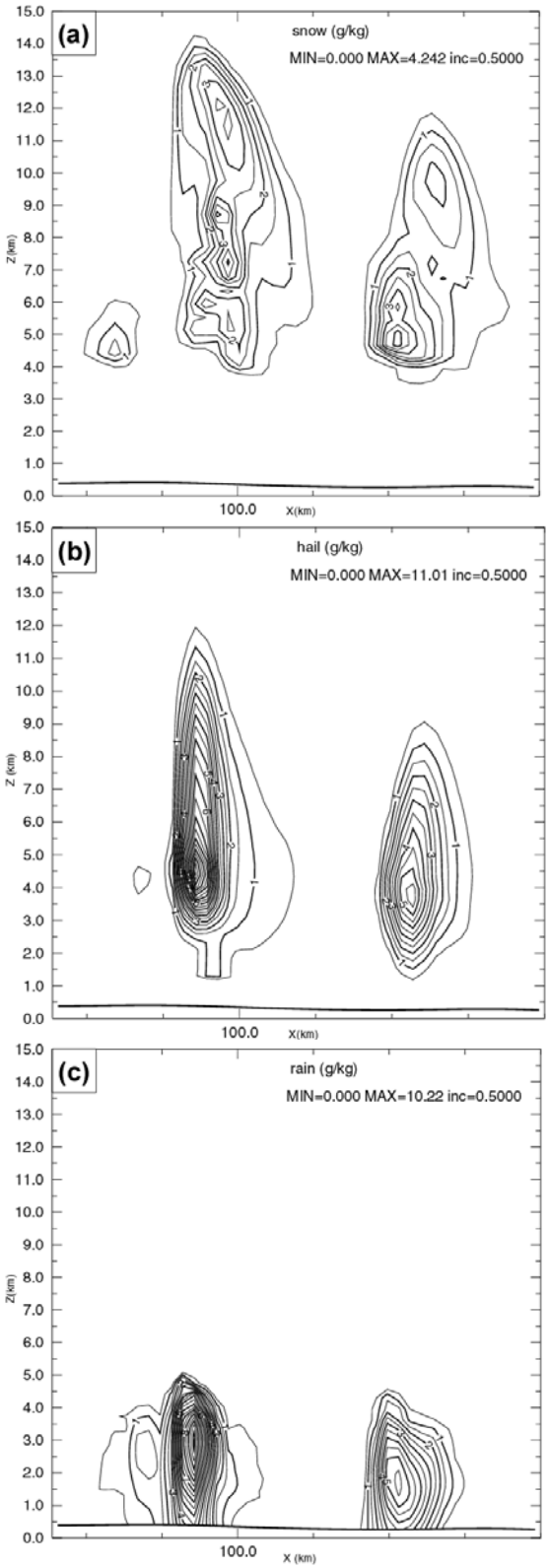

Fig. 3. Cross section of final analysis of snow, hail, and rain fields by the old cloud scheme.

3) Assigning the final values of precipitation species

In general, analyses for numerical weather prediction are calculated as a sum of background values and analysis increments due to observations, weighted by factors related to the error variances of background and observation. Precipitation fields are, however, not continuous variables therefore require a different scheme to determine the final analysis quantities, reconciling the background quantities and the observations. In the old scheme, the final analysis of precipitation species is the greater of the background and observed quantities. This was a legacy from LAPS which had been developed using a mesoscale Rapid-Update-Cycle (RUC) model forecast as the background field, not a storm-scale model forecast. In new scheme, the analysis takes the values retrieved from the observations, except in the area of missing observations and outside the radar observing range, where background values are then used for the precipitation mixing ratios. This approach is more appropriate when using storm-scale forecasts as the background as we do inside assimilation cycles. Choosing the observation over the background is based on the belief that radar observations of precipitation are much more reliable than that predicted by a numerical model. Furthermore, at the storm scale, reliable information about the background error, especially that of precipitation fields, is generally unavailable.

We demonstrate the effect of the above procedure, by examining the analyses for a situation using a 3-km 10-minute ARPS forecast as the background field and radar data at 22:50 UTC on March 28, 2000 in the Fort Worth, Texas area. The final analysis of precipitation species by the old scheme is plotted in Fig. 3. Compared to the retrieval (Fig. 2, left column), it can be seen that with the old scheme the background values dominate the final analysis for all three species **(**Fig. 2**).** The reflectivity fields calculated from the precipitation mixing ratios of the background, the final analysis of old scheme and new scheme are plotted in Fig. 4. We can see that analyzed reflectivity from the old scheme largely reflects the background, while the analyzed reflectivity using new scheme shows many detailed structures inside the storms.

b. The cloud water and cloud ice

To estimate cloud water and cloud ice, the adiabatic liquid water content (ALWC) is estimated by assuming moist-adiabatic ascent from

cloud base to cloud top. Then a reduction is applied to the ALWC to account for entrainment. In old scheme, the curve of reduction was determined from field data that was collected largely from isolated towering cumulus clouds. In a case with supercell thunderstorms or widespread thunderstorms, the clouds have much larger vertical extent and less entrainment in the center of storm cells. So a new entrainment curve is devised for the new scheme to provide greater cloud water and cloud ice content. Fig. 5 shows analysis of cloud water and cloud ice using the old curve (left) and the new curve (right) with reduced entrainment. The increased cloud mixing ratios are quite evident. In the current 3-km grid system, we have noticed that the initial cloud water and cloud ice are sufficient to sustain the cloud and precipitating convective cells for 10 to 15 minutes into the forecast and the continued sustenance requires cloud water and cloud ice be generated by continued condensation of moisture, generally due to moist-air lifted from the boundary layer.

c. In-cloud thermal adjustment

In the old scheme the incremental buoyancy added due to the added cloud water and precipitation is calculated from the latent heat released by the incremental cloud water and ice. In new scheme, a moist-adiabatic temperature profile with the same entrainment factors as applied to the cloud water, is used to adjust temperature after the determination of cloud and precipitation content. The new in-cloud temperature adjustment scheme is more consistent with the physics of a convective storm because it reflects the temperature change in an ascending bubble of moist air. The typical temperature increments from the adjustments of new and old schemes are plotted in Fig. 6. The profile of horizontally averaged temperature increments show that the new method heats atmosphere through a greater depth than the old method, while the old scheme acts to warm the atmosphere more in middle and low layers because the added cloud water and ice tend to be concentrated in these layers (Fig. 6a). The difference in the temperature increment between the two schemes at 4.5 MSL in Fig. 6b reflects the main structures of observed reflectivity (not shown).

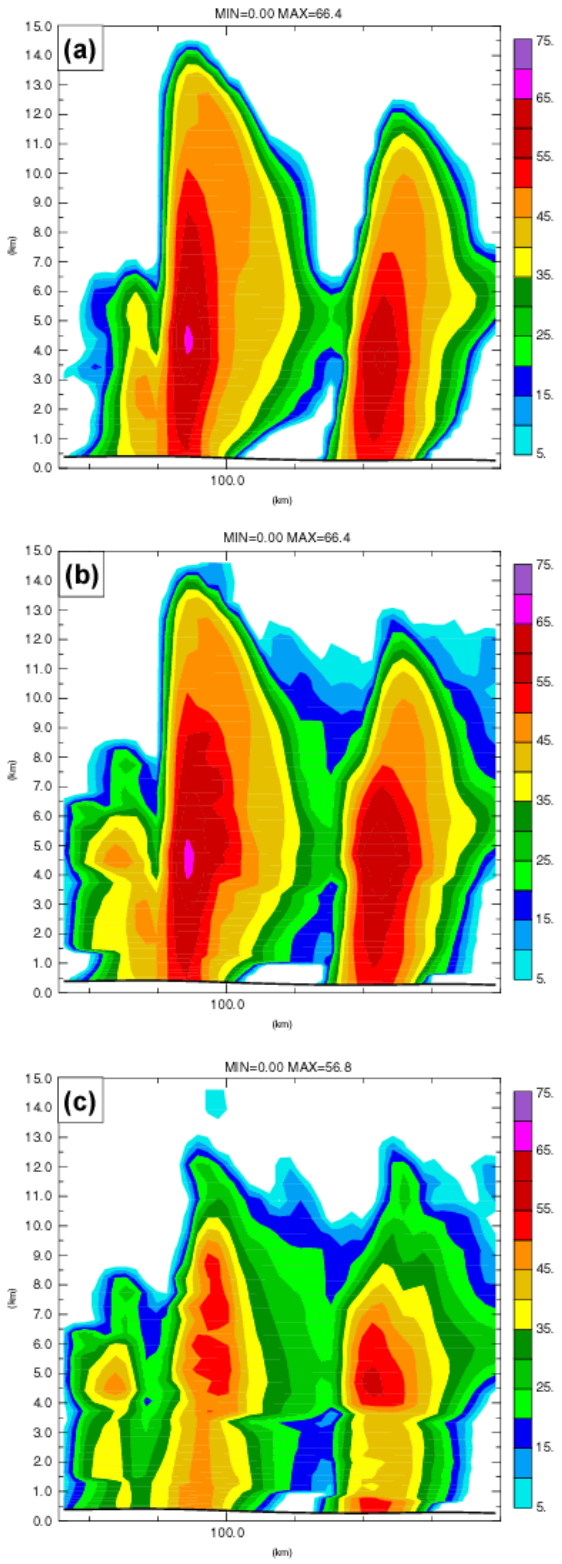

Fig. 4. Cross section of reflectivity fields calculated from precipitation mixing ratios of: a). background; b). analysis of the old cloud scheme; c) analysis of the new cloud scheme.

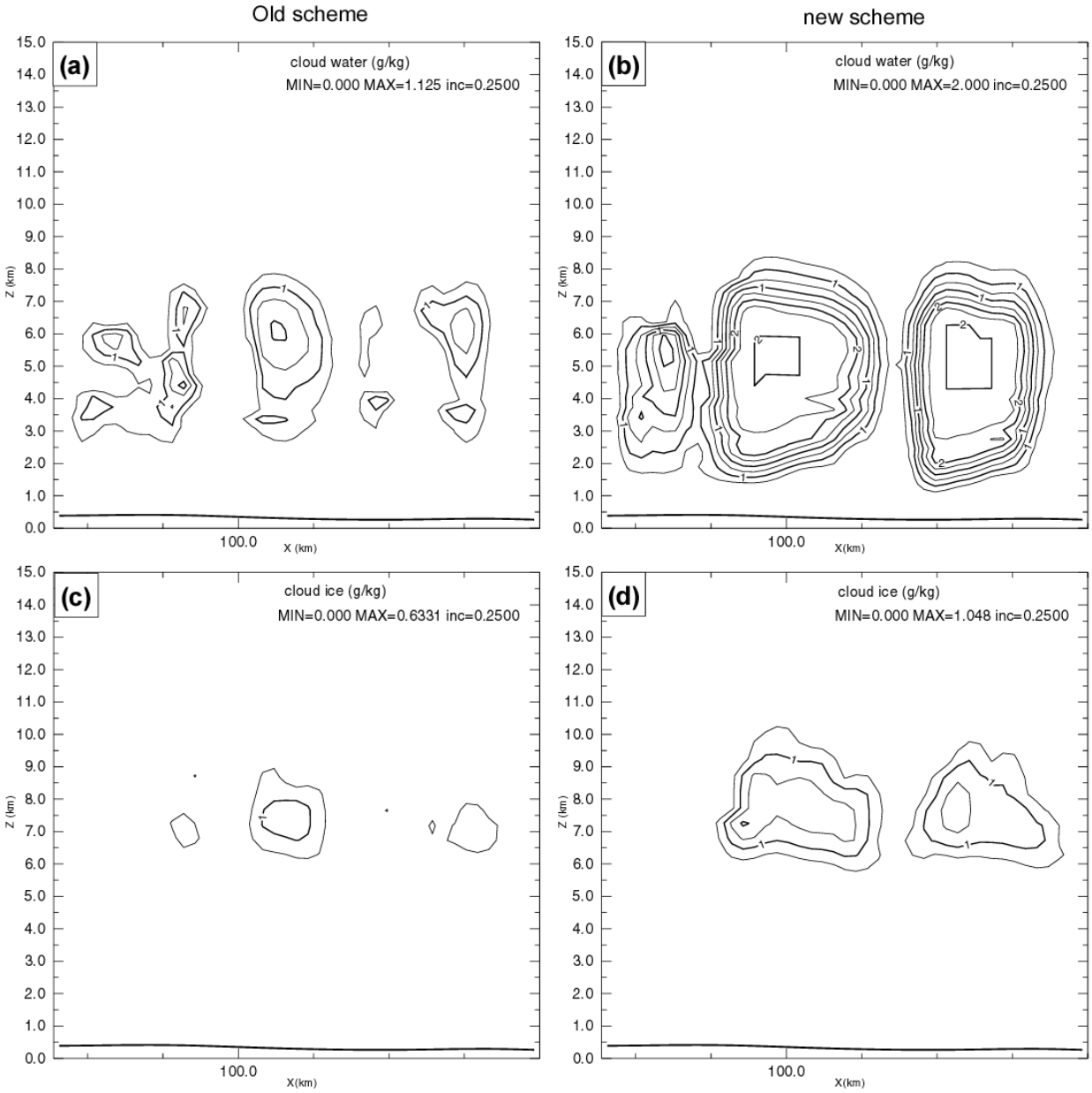

Fig. 5. Cross section of cloud water and cloud ice fields from analysis using the old curve (left) and the new curve (right) with reduced entrainment.

4. FORT WORTH TORNADO CASE AND DESIGN OF FORECAST EXPERIMENTS WITH ARPS

As stated earlier, in this study, we apply our 3DVAR and cloud analysis system to the Fort Worth tornado case studied by X03. We evaluate the performance of the system by examining the quality of assimilation results and subsequent forecast. On March 28, 2000, two tornadoes touched down in the Fort Worth, Texas (TX) area. One reached F2 intensity (maximum winds 51 ms^{-1} to 70 ms^{-1}) and struck downtown Fort Worth at around 6:15 pm LST March 28, 2000 or 00:15 UTC March 29. The tornado funnel developed directly over the city, descended, and stayed on the ground for at least 15 minutes. The tornado caused extensive damage to several structures, including high-rise buildings. It directly caused two fatalities and many injuries. The parent storm also brought torrential rains and softball-size hail stones, causing two deaths from flooding in the

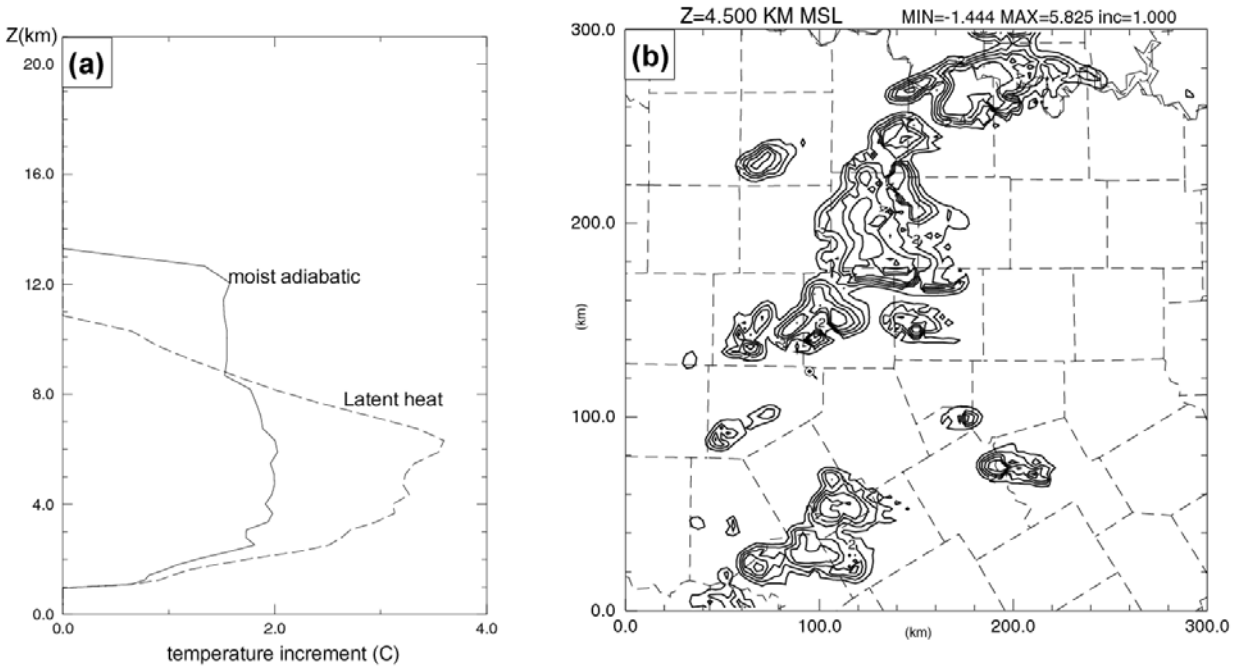

Fig. 6. a). The profile of horizontally averaged temperature increments from adjustments of the new (moisture adiabatic profile) and old (latent heating) schemes; b). the difference in the temperature increment between the old and new temperature adjustment schemes at 4.5 MSL.

eastern portion of Tarrant County (highlighted in Fig. 7), near Arlington, and one additional death due to hail. Another tornado from the same complex of storms touched down in south Arlington, some 25 kilometers east of Fort Worth, about 30 minutes after the Fort Worth tornado, at about 6:45 pm LST March 28, 2000 (00:45 UTC March 29). These tornadoes have special significance because they struck the center of a major metropolitan area.

The mesoscale and synoptic scale settings in which the tornadic thunderstorms occurred are described in X03. The primary goal of this work is to test the impact of Level II WSR-88D reflectivity and radial velocity data on the ability of a high-resolution model and its data assimilation system to initialize and forecast pre-existing thunderstorms. The capabilities of the ARPS 3DVAR and the improved cloud analysis procedure are also examined through real case experiments. Because all thunderstorms to be studied occurred within the range of Fort-Worth (KFWS) radar during the period of assimilation, only data from KFWS are used. The reflectivity data from the same radar will also be used to verify the model forecast.

Similar to the experiments reported by X03, two levels of one-way nested grids are used here, with the resolutions being 9 and 3 km, respectively. The two grids cover areas of 1000 ×1000 and 450×300 km^2, respectively, and the vertical grid spacing is increased from 20 m at the surface to about 770 m at the model top located at 21.1 km height**.** The model settings are essentially the same as in X03, except that an updated version of ARPS is used. Specifically, we employ full model physics, including a two-layer soil-vegetation model and Lin et al (1983) ice microphysics. Cumulus parameterization is not used on either grid. The 9-km grid is initialized at 18 UTC March 28, from a single 3DVAR analysis that combined rawinsonde, wind profiler, NWS surface and Oklahoma Mesonet data, using NCEP Eta 18 UTC analysis as the background. At the lateral boundaries, the 9-km grid is forced by the Eta 18 UTC forecasts at 3-hour intervals. No data assimilation is performed for the 9-km grid and the forecast is run for 12 hours, ending at 06 UTC March 29. With the primary goal of initializing pre-existing storms, the 3-km grid is started at later times, when some of the thunderstorms have already formed and been observed by the WSR-88D Doppler radars.

Different from the 3-km experiments of X03, we use the ARPS 3DVAR instead of ADAS as the analysis tool. Further, we use an improved ver-

sion of ADAS cloud analysis; some of improvements are described in Section 3 and Brewster (2002). In addition, we use Level II instead of Level III data with 10-minute instead of 15-minute intermittent assimilation cycles. As in X03, the hour-long assimilation period starts at 22 UTC and end at 23 UTC, about 1 hour 15 minute before the tornado touched down in Fort Worth. The Level II data contain 9 (in the first half an hour) or 14 (in the second half an hour) instead of 4 elevation scans, and without Level III's degradation in the radial velocity data precision (Level-III radial velocity data were used in X03 through a simple radial velocity adjustment procedure of ADAS). The reflectivity data are used in cloud analysis procedure to retrieve cloud and hydrometers fields and to make adjustments to in-cloud temperature and moisture. The radial velocity data are analyzed by the 3DVAR subjecting to a mass continuity constraint.

Since data representing very different spatial scales are used, we employ the multi-pass strategy available with our 3DVAR system. Specifically, three analysis passes are performed on the 3 km grid, with each pass using different data types. For the wind profiler data used in the first pass, a 120 km filter scale is used. Filter scales of 75 and 9 km are used in the second and third passes when surface data and radial velocity data are used, respectively.

The 3-km forecasts start at 23 UTC March 28 from the assimilated initial conditions and end at 02 UTC March 29. Because few surface and upper-air data are available within the 3 km domain during the assimilation period, the storm environment is defined primarily by information carried-over from 18 UTC (when there are more observations) by the 9-km ARPS forecast or from even earlier by the Eta model. The 9-km preforecast period is generally helpful in reducing the spin-up time on the 3-km grid for both the assimilation and model forecast.

Table 1. List of 3 km experiments on the use of radial velocity and their main characteristics.

Experiment	Use of Reflectivity	Use of Radial velocity	Mass continuity constraint	
			Dimension	Weighting Coefficients
CNTL	Yes	Yes	2D	$\alpha\lambda_c$ =1000, β=0
CLD	Yes	No	N.A.	λ_c =0
VR	No	Yes	2D	$\alpha\lambda_c$ =1000, β=0
NoVRZ	No	No	N.A.	λ_c =0
NoDiv	Yes	Yes	N.A.	λ_c =0
Div2Da	Yes	Yes	2D	$\alpha\lambda_c$ =500, β=0
Div2Db	Yes	Yes	2D	$\alpha\lambda_c$ =2000, β=0
Div3Da	Yes	Yes	3D	α λ_c =1000, β λ_c =100
Div3Db	Yes	Yes	3D	$\alpha\lambda_c$ =β λ_c =1000

Table 2, The list of 3km experiments on new cloud analysis and their main characteristics.

NAME	Temperature adjustment	Precipitation analysis	Retrieval precipitation	Radar Data
CLD	Moist adiabatic profile	Retrieval value	SMO	Level II
X03	Latent heat	Maximum of retrieval and background	KRY	Level III
CTLH	Latent heat	Retrieval value	SMO	Level II
CMAX	Moist adiabatic profile	Maximum of retrieval and background	SMO	Level II
CKRY	Moist adiabatic profile	Retrieval value	KRY	Level II

In this paper, results from thirteen experiments, including a control, are reported. Nine of these experiments are designed to specifically investigate the impact of assimilating radial velocity data (see Table 1) and four of them to examine the impact of reflectivity data and the improved cloud analysis procedure (see Table 2). The control experiment, CNTL, includes both Level II reflectivity and radial velocity data in its assimilation cycles. A two-dimensional version of mass continuity constraint is imposed in the 3DVAR analysis. Three of the other experiments in table 1, namely CLD, VR and NoVRZ, examine the effect of including reflectivity (denoted as Z), radial velocity (denoted as V_r) data alone or including none of them. The experiments are otherwise the same as CNTL.

The next five experiments in table 1 are designed to examine the role and effect of various formulations of the mass continuity constraint in the 3DVAR cost function. They are different from CNTL in the use of mass-continuity constraint. Experiment NoDiv does not include a mass continuity constraint while experiments Div3Da and Div3Db use a three-dimensional mass-continuity constraint. The weighting coefficients of horizontal and vertical part of the mass divergence terms are different in Div3Da but the same in Div3Db. Experiments Div2Da and Div2Db are conducted to test the sensitivity of storm forecasts to the magnitude of weighting coefficient of two-dimensional mass continuity constraint and the values of the weight coefficient are listed in Table 1.

In the five prediction experiments that are conducted to study the impact of the improved cloud analysis procedure, experiment CLD is also listed in table 1 as a comparison to study the impact of radial velocity. It employs reflectivity data only in the assimilation cycles and the 3DVAR analysis is used to analyze model state variables in data assimilation but no radial velocity data are employed in its wind analysis. The control experiment of X03 is repeated for comparison (listed as experiment X03 in Table 2). Based on CLD, three experiments, CTLH, CMAX and CKRY are performed to examine the impact of different schemes of in-cloud temperature adjustment, final precipitation species assignment rules and the retrieval of precipitation species values in the old and new cloud analysis procedures (Table 2).

We will focus our discussion on the quality of forecast during the one hour period spanning these tornado outbreaks, i.e., from 00:00 UTC to 01:00 UTC March 29, 2000.

5. RESULTS OF ASSIMILATION AND FORECAST EXPERIMENTS

In this section, we first discuss the results of control experiment CNTL by comparing the forecast radar reflectivity fields to the observed ones. The forecast results from experiments CLD and X03 are then analyzed to investigate the impact of the new cloud analysis procedure and the radial velocity, respectively. Further, Experiments VR and NoVRZ are described to examine the impact of radial velocity data on the storm prediction specially. The results from the experiments with different formulations of mass continuity constraint are also discussed. Finally, the impacts of each modification in the new cloud analysis procedure are then examined by comparing assimilation and forecast results of five experiments in table 2.

a. Radar observations and results of control experiment

Since both tornadoes occurred between 00:00 UTC and 01:00 UTC March 29 in the Fort Worth area, we focus our discussion of the forecast on this period. The quality of forecasts up to 01:00 UTC will also be briefly discussed. For direct comparison with radar observations, we derive reflectivity from model-predicted hydrometeor fields that also take into account of the ice phases, and the reflectivity equations follow mostly Smith et al. (1975), which can also be found in Tong and Xue (2004). The predicted reflectivity fields from the control run, which included both reflectivity and radial velocity data, are mapped to the 1.45° radar elevation level of KFWS radar (marked in the plots) and are plotted in the right column of Fig. 7 at 15 minute intervals for a 1 hour period starting from 00:00 UTC March 29 while the corresponding observed reflectivity fields from the KFWS radar are plotted in the left column of the same figure. Fort Worth and Arlington are marked in Fig. 7b.

At 00:00 UTC March 29, five individual thunderstorms can be identified near Forth Worth from the radar observations (Fig. 7a). They are labeled A, B, C, C' and D in the plots. Storm A is the storm that spawned the downtown Fort Worth tornado at around 00:15 UTC and the Arlington tornado 30 minutes later. Storm B approached Storm A from the west, during the period 00:00 UTC to 00:45 UTC (Fig. 7a, c, e, g) and then merged with Storm A to form a combined storm that we re-label as F (Fig. 7i) at 01:00 UTC. Storms C and C' formed near the end of the as-

similation window, propagated towards Storm A from the south and also merged with Storm A (Fig. 7a, c, e, g, i) by 01:00 UTC. Storm D was initially located near the northeast corner of Hill County (see Fig. 7) and later propagated northeast into Ellis County. Storm D was initiated during the assimilation window and remained strong throughout the period of tornadoes. The complex interactions among these storm cells pose a major challenge for accurate forecasting of the morphology of these storms.

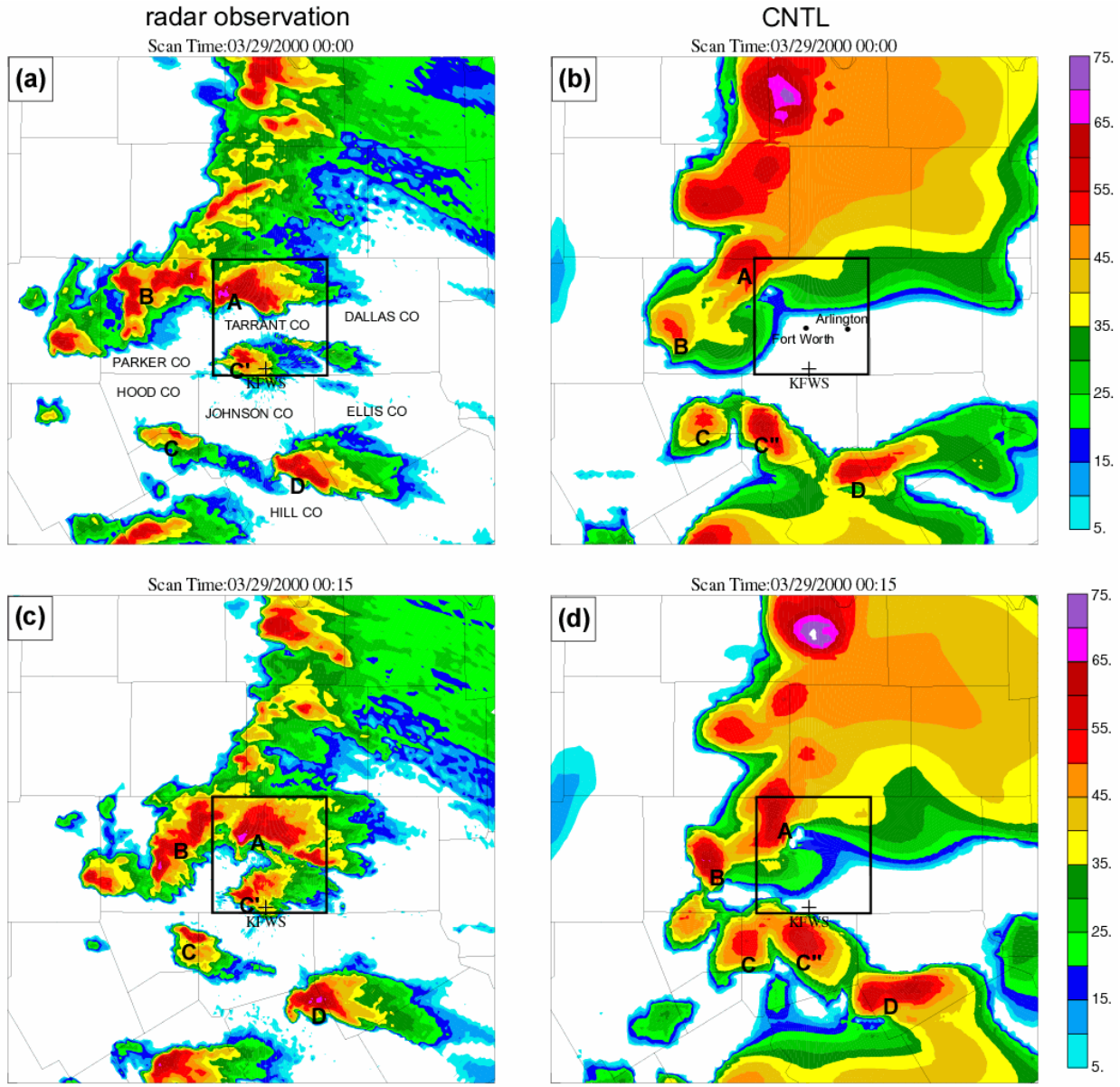

Fig. 7. Observed reflectivity fields at 1.45° elevation of the Fort Worth radar (marked as KFWS) based on Level-II data (left column), and predicted reflectivity at the same elevation from control experiment CNTL (right column), at 15 minute intervals from 00:00 UTC to 1:00 UTC March 29, 2000. Major storm cells are marked by capital letters. Fort Worth and Arlington are marked as dot in (b). Tarrant County is highlighted and about 50×50 km^2 in size. The domain shown is about 200 km on each side, representing the portion of 3 km grid between 100 and 300 km in east-west direction and from 60 to 260 km in north-south direction. Counties around Fort Worth are marked in (a).

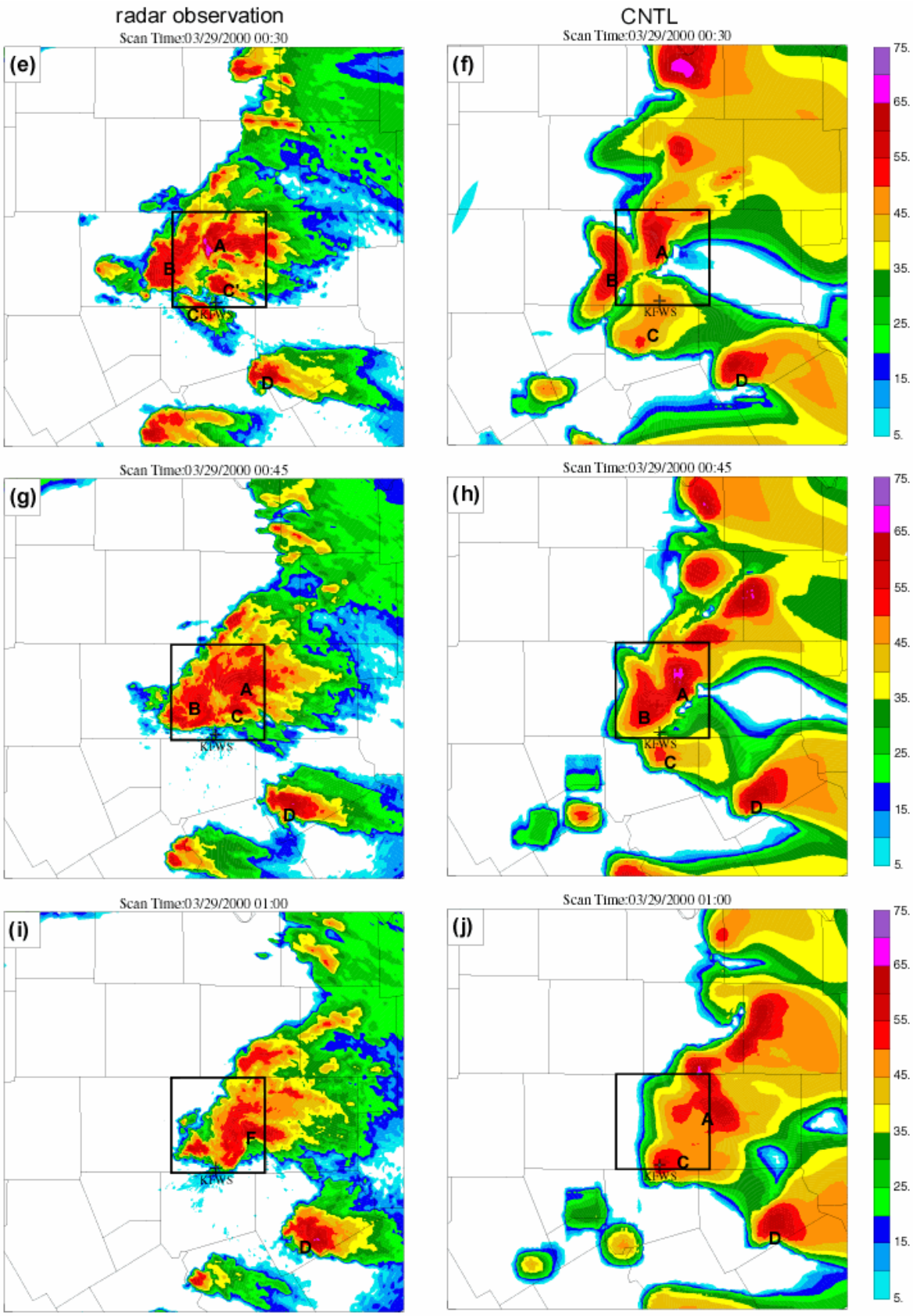

Fig. 7. Continued.

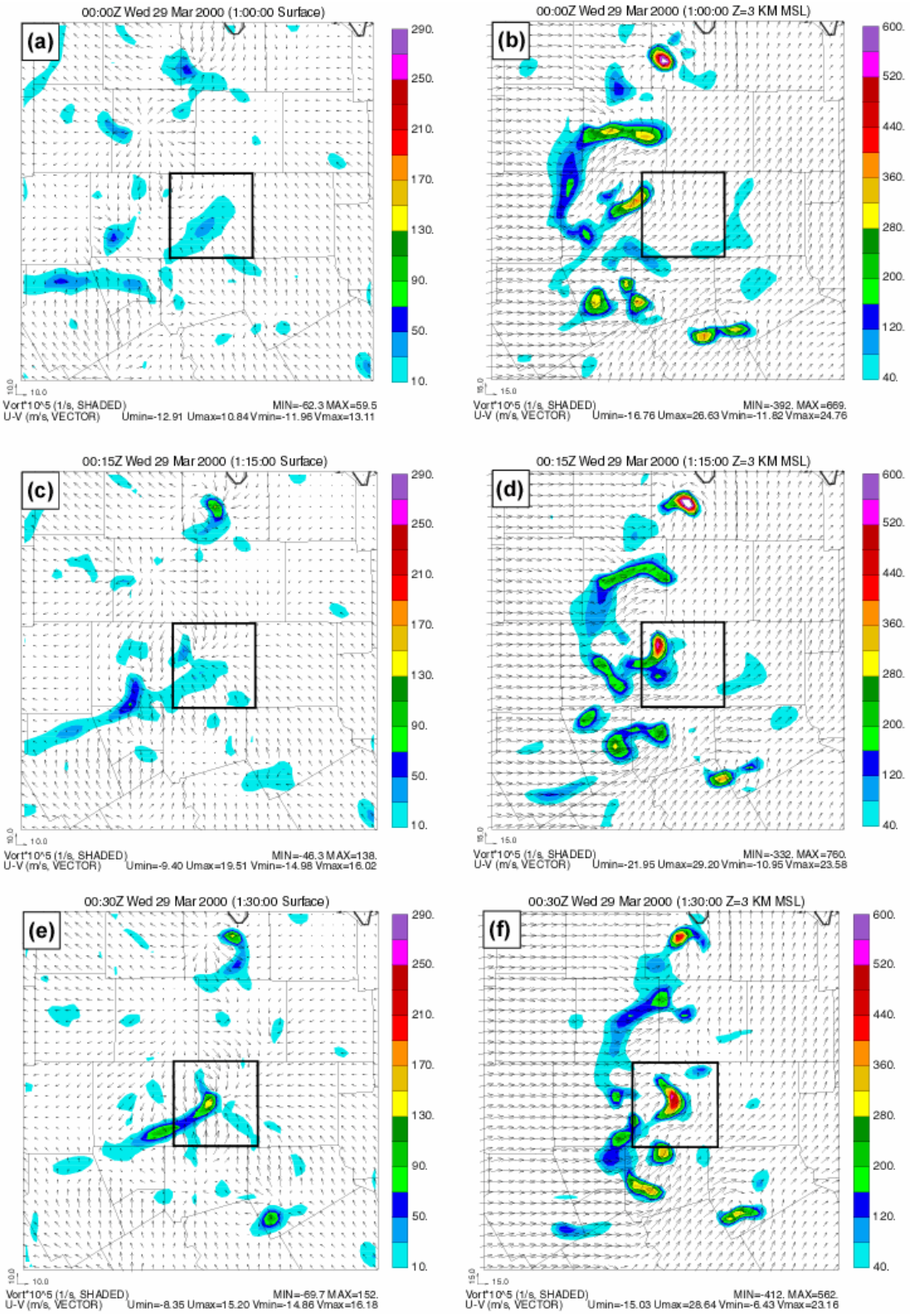

Fig. 8. Predicted wind and vertical vorticity fields at the surface (left column) and 3 km MSL (right column) from control experiment CNTL corresponding to the times of Fig. 7. The domains shown are the same as in Fig. 7.

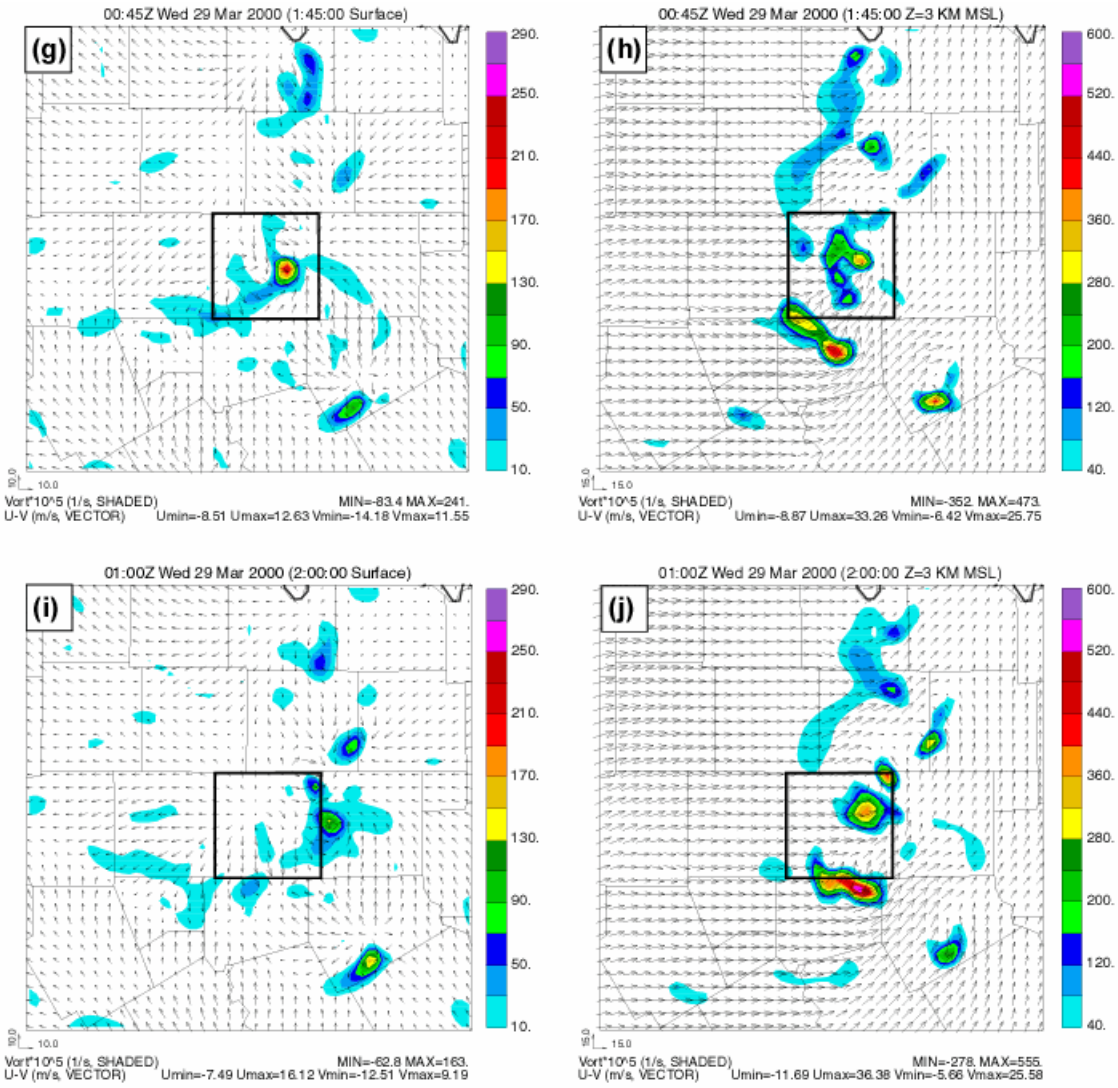

Fig. 8. Continued.

The model forecast at 00:00 UTC March 29, also depicts five storm cells in the vicinity of Fort Worth (Fig. 7b). Four of them can be directly linked to an observed one (Fig. 7a), but the one labeled C" has no real world counterpart. Storms A and B have location errors of about 20-25 km while the locations of Storms C and D have position errors of less than 5 km. Observed Storm C' is missed by the forecast at its location near the southwest corner of Tarrant County while the model placed a storm cell, C", further to the south, in west-central Johnson County. When we examine the forecast during the first hour (23:00-00:00 UTC, not shown here), it is found that all storm cells that existed at the beginning of forecast underwent varying degrees of adjustment. Storms A and B weaken initially and grow again from 23:45 UTC, while Storm C remains relatively weak until about 23:50 UTC. Given that little information on Storm C was provided by the radar or the assimilation process, the model did a good job in initiating Storm C. Apart from some error in propagation speed (a little too fast), Storm D is very well predicted throughout the period by the model. Both the observed and predicted low-level reflectivity of Storm D show clear hook echo shapes although no tornado was reported within this storm. Fig. 8 shows the predicted wind vector and vertical vorticity fields from the control experiment at the surface (left column) and 3 km MSL (approximately 2.8 km AGL, right column) at the same times as the reflectivity fields shown in Fig. 7. From the surface wind field at 0:00 UTC, strong and fairly isolated convergence centers

are indicated for Storms A, B and D (Fig. 8a). The gust fronts associated with the downdrafts of storms A and B are still relatively weak at this time while a much stronger downdraft is found to the northwest of A, associated with a storm that is decaying. Vertical vorticity associated with A is still weak at the surface. In the flow field at the 3 km MSL, however, a strong vorticity maximum is found within Storm A (Fig. 8b).

Fifteen minutes later, at 00:15 UTC, the time of Fort Worth tornado outbreak, both predicted Storms A and B are enhanced significantly (Fig. 7d). The location error of the maximum reflectivity center of Storm A is reduced significantly, to within 10 km of the observed one (Fig. 7c, d). The predicted locations of B and C are also very accurate at this time. Spurious Storm C" remains and appears as a strong reflectivity center. Storm D moved east a little too fast in the 15 minute period, with the reflectivity core entering Ellis County by this time. The wind fields exhibit a strong convergence center and a weak vorticity center at the surface (Fig. 8c) but a strong vorticity center at 3 km MSL (Fig. 8d) associated with A. The convergence and vorticity centers related to Storm B are also enhanced. A new spurious storm south of Storm B is generated by collision of gust fronts from Storms B and C (Fig. 7d and Fig. 8c). These results show that the main Storm A is predicted with high low-level reflectivity and strong mid-level rotation and approaches Fort Worth city from the northwest. Despite some delay in the intensification of low-level rotation in the forecast, it contains clear indications for the potential of a tornado from this cell.

In reality, an F2 tornado spawned from Storm A struck downtown Fort Worth from 00:15 UTC to 00:30 UTC. At 00:30 UTC, the control forecast gives good indications, in both reflectivity and wind fields, of possible tornadogenesis from Storm A. The predicted reflectivity matches very well with observation (Fig. 7e, f). The south flank of predicted storm is sweeping through Fort Worth city consistent with the observations at this time. The weaker surface vorticity center found in Fig. 8c earlier has developed into a strong vorticity center by 00:30 UTC, with a maximum value of about $1.5\times10^{-3}s^{-1}$ (note that the grid resolution is a coarse 3 km), and the maximum is located almost right over Fort Worth (Fig. 8e). Collocated with the vorticity maximum is also strong surface convergence, indicating the presence of strong near-surface updraft and associated vertical stretching. An isolated maximum vorticity center within Storm A is even better defined at 3 km MSL (Fig. 8f) but it is not as strong as it was at 00:15 UTC. The intensification of ground level vorticity and slight weakening of mid-level rotation suggest shifting of strong rotation to the lower levels, which typically occurs during tornadogenesis and in the later life cycle of tornadoes (see, e.g., Davies-Jones 2001). The development of this strong, well-organized, deep vorticity column during the period that coincides with the Fort Worth tornado indicates good fidelity of the predicted storm, even though the model resolution is much too coarse to produce flow on the scale of a tornado or even the tornado's parent vortex.

At 00:30 UTC, Storm B is also reproduced well by the forecast as seen from the reflectivity field. The spurious storm cell to its south found at 00:15 UTC has merged with Storm B by this time. The vorticity center related Storm B is much weaker than that of Storm A at both the surface and 3 km MSL. Predicted Storm C covers the area of observed Storms C and C' and there is no identifiable surface vorticity center associated with it. Predicted Storm D is located northeast of the observed one by about 10 km because of its faster northeastward propagation. At this time, the main characteristics of the storm cells A through D are all very accurately predicted by the model, and the representations are an improvement over that reported in X03.

At around 00:45 UTC, another tornado occurred in south Arlington. The forecast valid at this time also indicates high potential of tornadogenesis at about the right place. By this time, the reflectivity core of Storm A has moved to eastern Tarrant County, near Arlington, and a well-organized, deep and stronger vorticity column is nearly collocated with Arlington (Fig. 7g, h and Fig. 8g, h). The surface maximum vorticity is now $2.4\times10^{-3}s^{-1}$, even higher than earlier. The model successfully predicts Storm B's decay and merger with Storm A around this time. The predicted Storm C lags behind the observed one by nearly half a county and does not merge with Storm A as the real one did. The forecast for Storm D matches the observed radar echoes well. At the surface, the northwest side of outflow of Storm D is approaching Storm A located to its northwest, which probably contributed to the weakening of Storm A and its subsequently merged storm.

In reality, Storms A, B and C merged together and formed Storm F at 01:00 UTC March 29 (Fig. 7i). The model has some success at forecasting this process, as the predicted Storms A and B did merge and Storm C's reflectivity field became combined with A and B's although its core remains separate by 01:00 UTC. Further, the pre-

dicted reflectivity maximum center has a displacement to the northeast (Fig. 7j). Predicted Storm D remains strong, as the observed one, and again is located slightly ahead of the observed storm. At the surface, maximum vorticity centers associated with the Storms A and D are still clearly identifiable (Fig. 8i), but is weaker with the former, which is consistent with the end of the Arlington tornado. At 3 km MSL, the disturbances and vorticity that appear to be associated with the decaying Storm C may be too strong (Fig. 8j); we do not have good data to verify their fidelity, however.

Based on the results of our control experiment, it can be concluded that starting from an initial condition that assimilated WRS-88D radar Level II data together conventional observations through 3DVAR and cloud analysis, the model is able to predict the timing, location and key characteristics of convective storms with very good accuracy. The accurate prediction of the development of a strong, well-organized, deep vorticity column associated with the tornadic storm in a period spanning the two observed tornado outbreaks is especially encouraging. Our results also show that when several storms are spaced closely, complex storm interactions can occur, through, for example, gust front collisions. Spurious cells can be triggered when such interactions are incorrectly or inaccurately handled by the model. Such a situation requires an accurate analysis of all aspects of the convective storms.

b. Results of experiments CLD and X03

1) The effect of the use of new cloud scheme

Predicted reflectivities at the same elevation angle and time as Fig. 7 but derived from CLD and X03 are plotted in Fig. 9. For convenience of comparison, the left column of Fig. 9 show results of X03, in which the old cloud analysis scheme with Level-III reflectivity is used, while the right column shows the counterparts from CLD, whose assimilation cycles employ the new cloud analysis with Level-II reflectivity. None of them use radial velocity in their 3DVAR wind analysis. The comparison of these two experiments indicates the effect of the new cloud analysis with Level-II reflectivity.

At 00:00 UTC March 29, the one-hour forecast of CLD exhibits reasonable structures of the storms around Fort Worth (Fig. 7a, Fig. 9b) but with some position errors. Predicted Storm A lags the observation about 20 km. Predicted Storm B only shows as a weak echo and lags observation about 20-25 km. The model produces Storm C with a northward displacement of about 5 km and does not produce Storm C'. Considering that little information on Storms C and C' was provided by the assimilation cycles directly, it is encouraging that the model produces Storm C by itself at this time. The model produces an accurate forecast of Storm D, but at the same time, it generates a spurious storm, D', which split from Storm D in the first hour of the forecast and moves north into the southeast corner of Tarrant County. Another spurious storm appears southwest of Storm A and is labeled as A'. Comparing these storms to their counterparts in X03 (Fig. 9a), they are stronger than those in X03 except for spurious Storm D'. At this time, X03 gives much better position forecast for both Storm A and B than CLD does. However, the forecast of X03 misses Storm C and C', and produces a spurious storm, A', southwest of Storm A.

Fifteen minutes later, at 00:15 UTC, is the time of first tornado touchdown, in downtown Fort Worth. Experiment CLD correctly predicts tornadic Storm A strengthening and approaching Forth Worth from the west, although the forecast reflectivity maximum of Storm A is still a little behind the observation (Fig. 7c and Fig. 9d). Predicted Storm B remains weak and lags the observation about 25 km. Predicted Storm C is located midway between observed Storms C and C'. Storm D is well reproduced by CLD and the spurious Storm D' that appeared earlier has dissipated by this time. The spurious Storm A' has grown and is still at southwest of Storm A. In comparison, the storms in X03 moved eastward too quickly in the period from 00:00 to 00:15 UTC and the reflectivity maximum of Storm A has completely passed downtown Fort Worth (Fig. 9c). A weak echo at the center of the western boundary of Johnson County gives the only hint of observed Storm C in the Experiment X03 forecast. Just to the west of predicted Storm C, spurious Storm A' has developed into a long band-shaped echo connected with Storm A and subsequently sweeps through the weak Storm C. Unlike CLD, spurious Storm D' in X03 remains as a strong northbound storm.

At 00:30 UTC, in the CLD forecast, Storm A is nearly collocated with the observed cell except that it extends too much in the north-south direction and has two maxima reflectivity centers (Fig. 7e and Fig. 9f). Its shape does suggest an inflow notch on its southeastern flank. At this time, Storm B is not identifiable as a separate storm, though the southwestern quadrant of Storm A and the northeastern corner of Storm A' overlay the position of Storm B. Predicted Storm C ap-

pears as a weak echo that covers location of observed Storm C and C'. There is reason to believe the CLD forecast is a bit fast with the merger of cells that occurs in Tarrant County. Storm D is well reproduced except that it moves a little faster than observation, and spurious Storm A' still exists with a strong reflectivity center. In the X03 forecast, intense reflectivity composed by Storm A and A' is found extending from Storm A in the NE corner of Tarrant County through the SW corner of the county and reaching the center of Hood County (Fig. 9e). This may be a malposition of Storm A – representing a 30 km displacement, possibly due to a merger with the spurious Storm D'.

At 00:45 UTC, a second tornado struck just south of Arlington. In the forecast of CLD, the main characteristics of Storm A are successfully reproduced (Fig. 7g, Fig. 9h). The predicted southern reflectivity maximum of Storm A has intensified and is just south of Arlington. Together with northern reflectivity maximum of Storm A and the westward-extending part of Storm A, the area of predicted Storm A covers the bulk of the combined area of observed Storms A, B and C. At this time, isolated spurious Storm A' is weak. Predicted Storm D is still in a position a few km southeast of the observed cell. In the X03 forecast, the Storm D' has merged with Storm A and makes the later skip into the center of Dallas County (Fig. 9g). The northeast part of Storm A' is at the same area as the south center of Storm A in CLD and nears south Arlington too.

By 01:00 UTC, observed Storms A, B and C had merged into one storm F (Fig. 7i). In CLD run (Fig. 9j), the location of Storm A corresponds to the correct location of observed storm F, while in the X03 forecast (Fig. 9i), Storm A has led the observed Storm F over half a county (35 km) and Storm A' covers part of Storm F, but its center deviates from the main part of observed F by 15 km. The position forecast for Storm D in CLD is also more accurate than that of X03 at this time.

The surface wind and temperature fields from CLD and X03 at the time of the tornadoes are plotted in Fig. 10. At time of the downtown Fort Worth tornado, or about 00:15 UTC, CLD predicts areas of strong convergence along the gust front produced by tornadic Storm A approaching downtown Fort Worth from the northwest (Fig. 10b), while in experiment X03, the convergence coincident with the gust front of Storm A is much weaker and has passed downtown Fort Worth (Fig. 10a). At the time of the Arlington tornado, 00:45 UTC, the gust front and low-level convergence related to Storm A are still strong and approach south Arlington in the CLD run (Fig. 10d). In X03 (Fig. 10c), the gust front of Storm A is weaker and Storm A has moved east of Tarrant County. Almost the entire county is covered by the cold pool of Storm A' at this time.

From the above comparison, it is found that using new cloud analysis procedure with Level-II reflectivity data through assimilation cycles improves the prediction of the tornadic thunderstorm in this case. In the CLD run, the tornadic thunderstorm A, appearing with strong reflectivity with strong low-level convergence centers, approaches and passes downtown Fort Worth and Arlington around the times of tornado occurrence, while in X03, the reflectivity center of Storm A and the related gust front move too fast and have obvious locations errors during the tornado touchdowns.

2) The impact of radial velocity

In this subsection, the results from experiment CLD are compared to that of CNTL to identify the impact of radial velocity on the forecast of thunderstorms for CLD are the same as CNTL except that CLD does not use radial velocity data from KFWS in its assimilation.

As above description, CLD reproduced the main characteristics of Storm A quite successfully during the period of the two tornadoes (compare Fig. 7c, e, g and Fig. 9d, f, h), although the location errors are somewhat larger than that of CNTL from 00:30 to 00:45 UTC (compare Fig. 7d, f, h and Fig. 9d, f, h). Both experiments also give similar forecast for Storm D and spurious Storm C''. Predicted Storm B in experiment CLD appears as a large area of weak reflectivity at 00:15 UTC and disappears after that time. Instead of merging with Storm B, Storm A is followed by and merges with a strong spurious Storm A', which is triggered by a collision of the gust fronts from Storms A, B and C'' at 00:15 UTC (Fig. 10b). The forecast of CLD also misses observed Storm C in this period. Overall, the forecast of CLD is clearly not as good as that of CNTL and the differences clearly demonstrate the positive impact of assimilating radial velocity data in CNTL.

The predicted wind and vorticity fields at the corresponding times are given by Fig. 11 for the surface (left column) and 3 km MSL (right column) at 15 minute intervals for a half hour starting from 00:15 UTC March 29. From the wind and vorticity field, the positive impact of radial velocity data can be seen more clearly. The well-organized, deep column of strong vorticity that develops near Fort Worth and moves to Arlington during this half hour in the forecast of CNTL does not exist in the

forecast of CLD (Fig. 8 and Fig. 11). CLD does not develop a strong surface vorticity center within Tarrant County, and the 3-km MSL vorticity maxima found at 00:15 and 00:30 UTC have larger displacement errors. By 00:45 UTC the 3-km MSL vorticity maximum is considerably weaker than the one depicted in the control experiment. The differences in morphology of these features indicate that the forecast of the wind fields has been improved significantly by assimilating radial velocity data via our 3DVAR analysis.

3) Equitable threat scores

To more quantitatively evaluate the quality of forecast, we calculate and plot the equitable threat scores (ETS, Schaefer 1990) of predicted reflectivity at the 1.45° elevation level for the 5, 10, 15 and 30 dBZ thresholds (Fig. 12). The same ETS commonly applied to precipitation fields is used here. We can see in Fig. 12 a tendency for the scores to decrease quickly in first hour of forecast then increase in second hour for all four

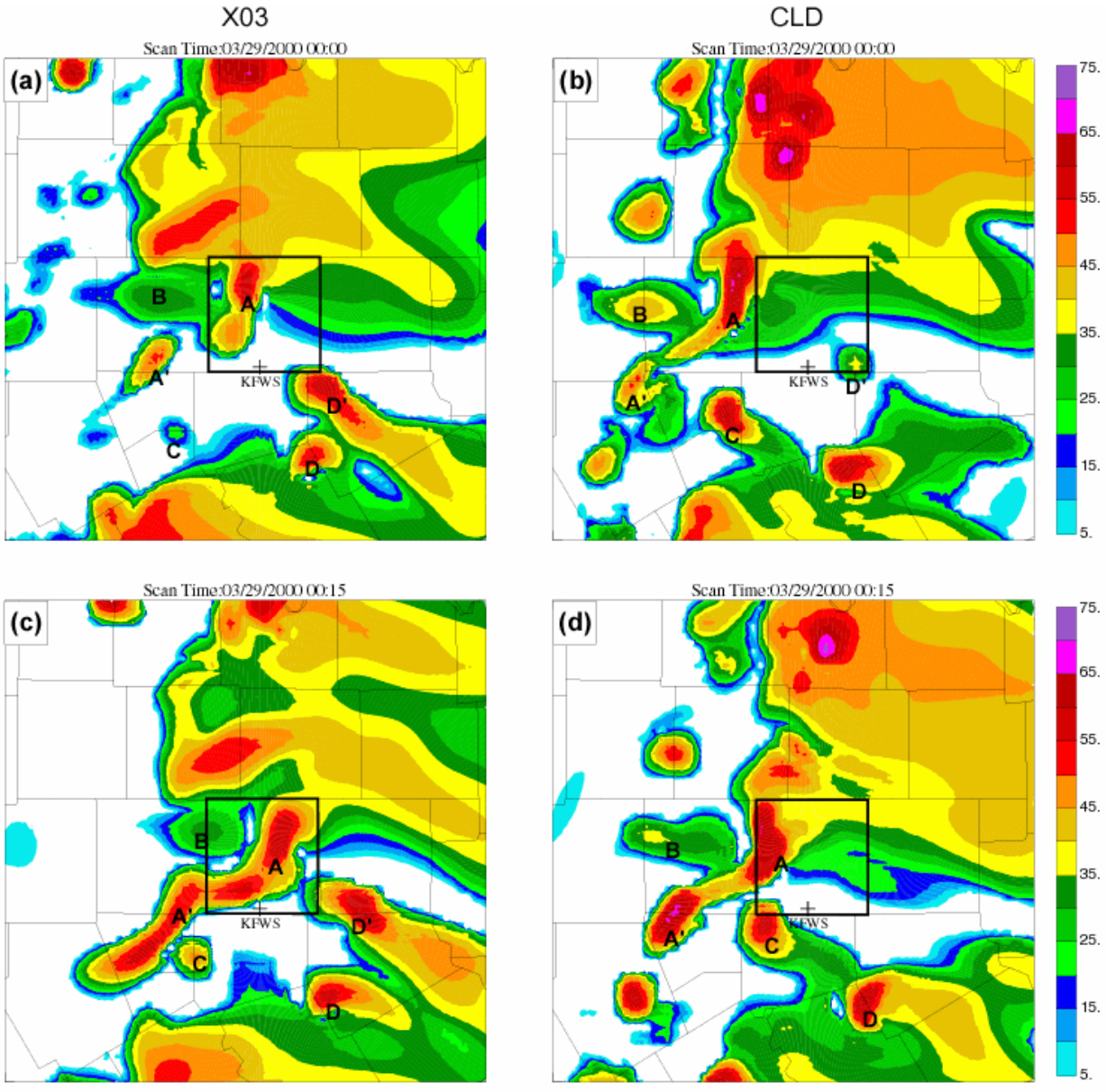

Fig. 9. Similar to Fig. 7, except that they are predicted reflectivity from experiments X03 (left column) and CLD (right column).

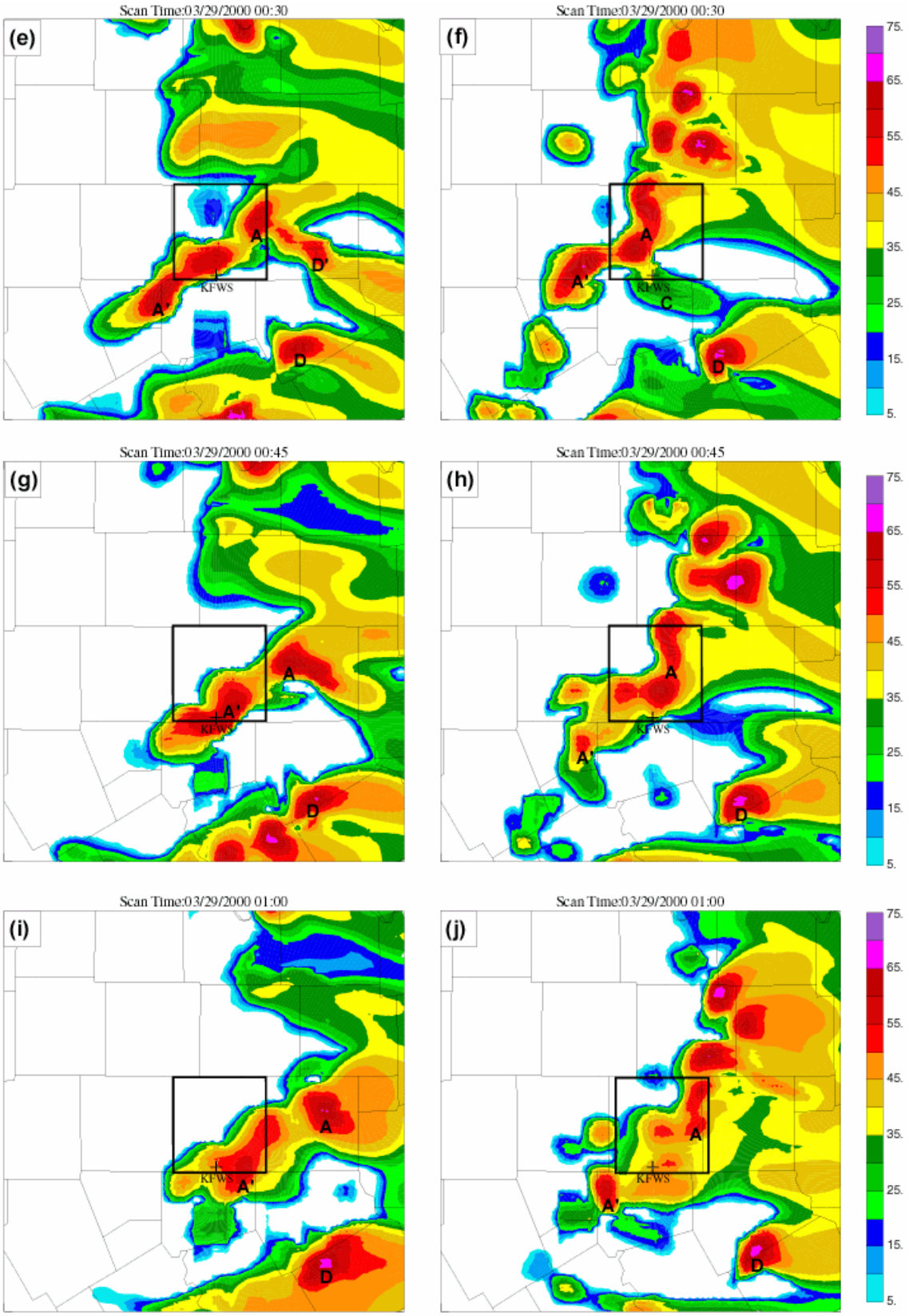

Fig. 9. Continued.

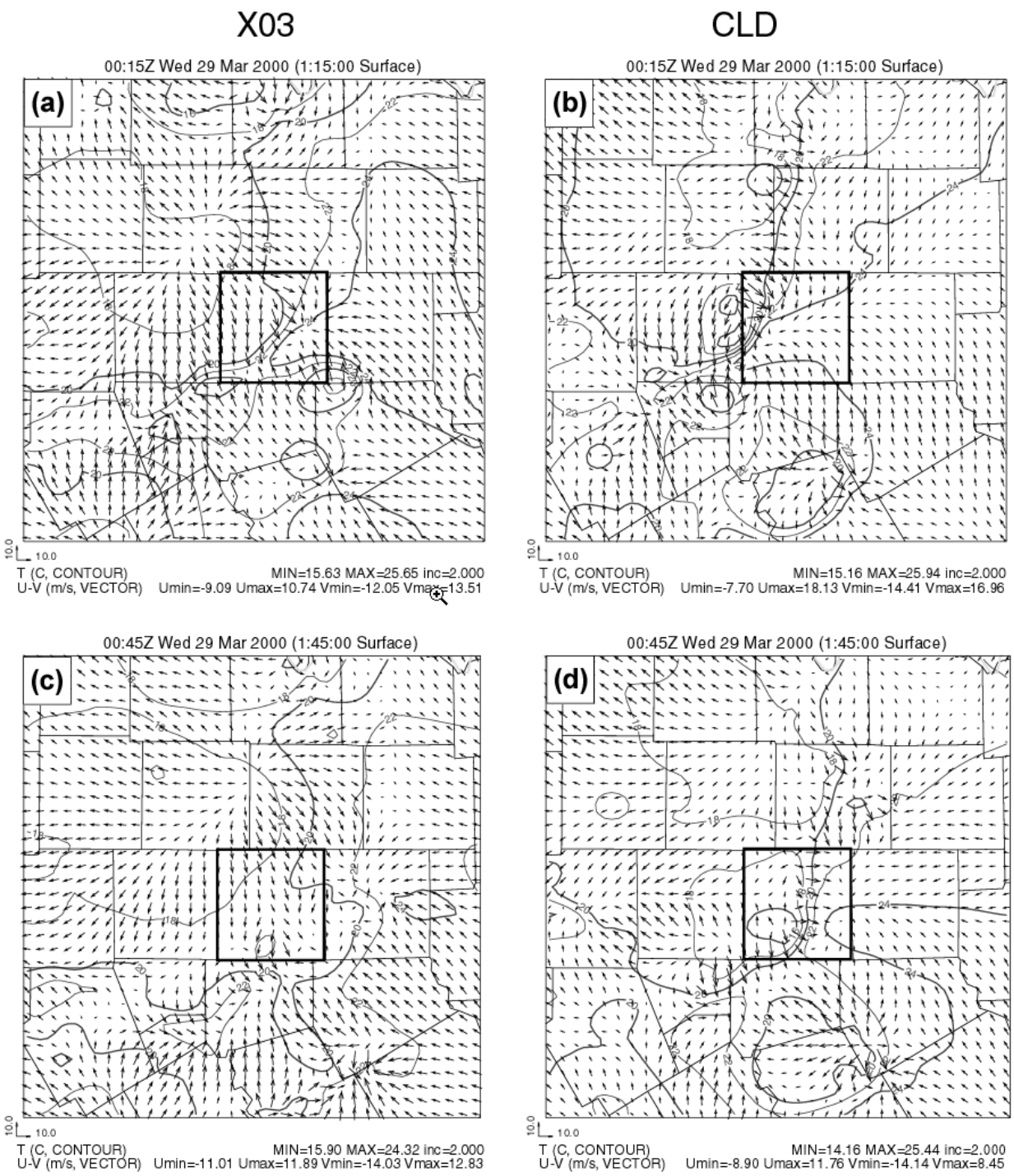

Fig. 10. Predicted surface wind and temperature fields from experiments X03 and CLD at 00:15 UTC and 00:45 UTC March 29, 2000. The domains shown are the same as in Fig. 7.

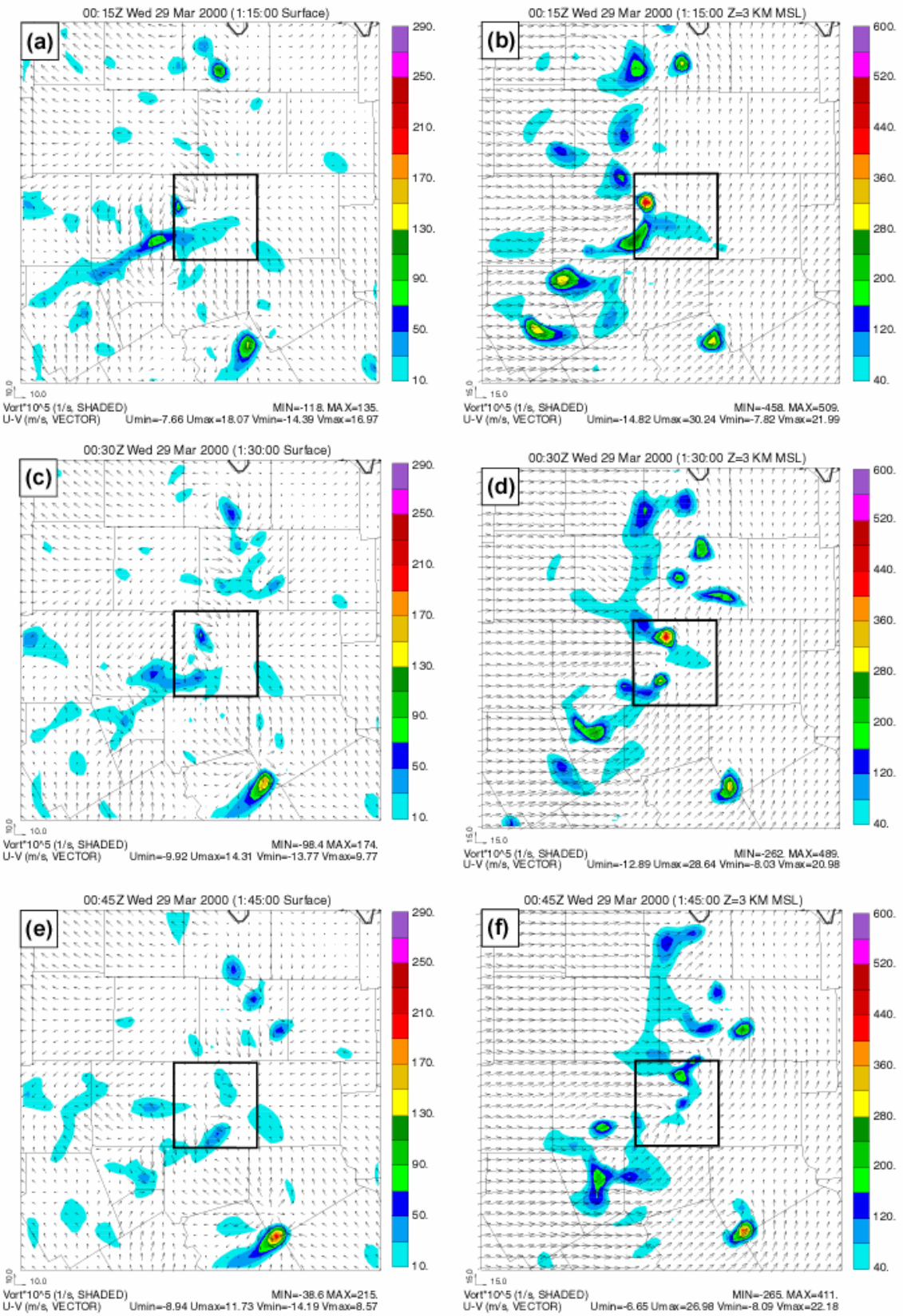

Fig. 11. Similar to Fig. 8, except that they are predicted wind and vorticity fields from experiment CLD at 15 minute intervals from 00:15 UTC through 00:45 UTC March 29, 2000.

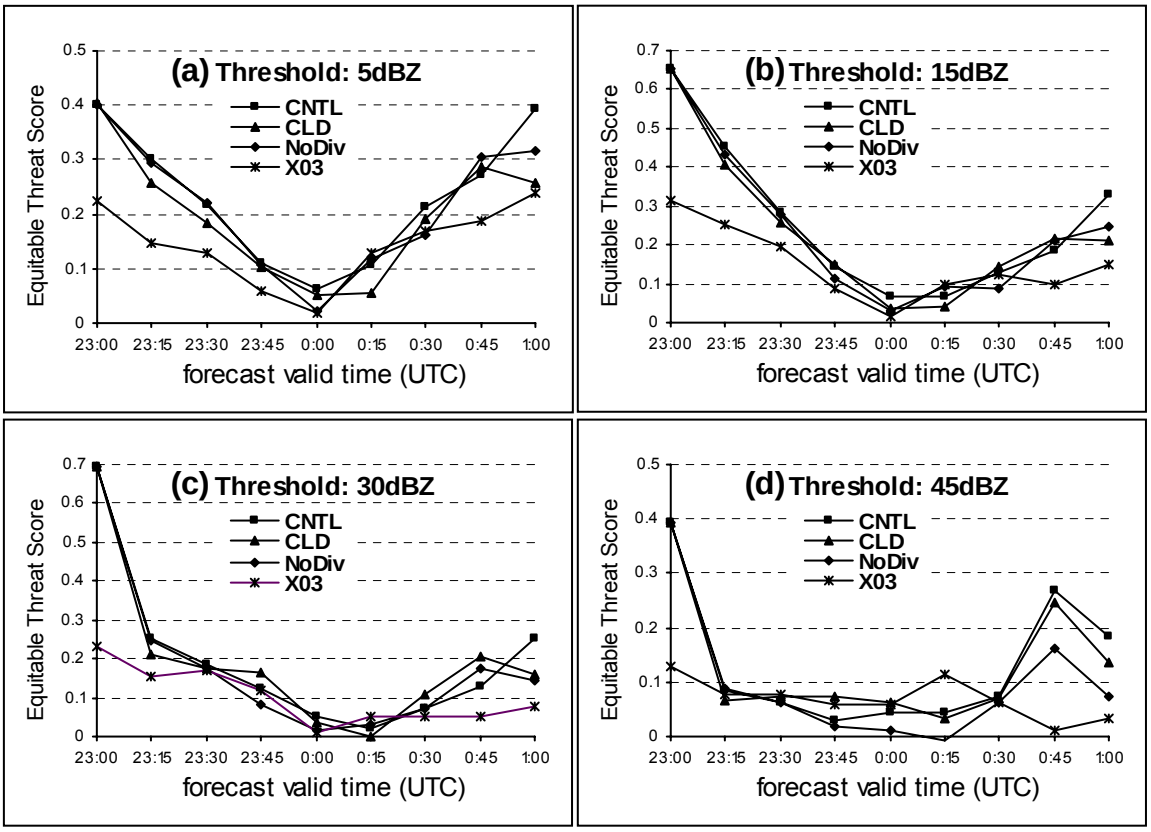

Fig. 12. Equitable threat scores of predicted reflectivity for the 5 dBZ (a), 15 dBZ (b), 30 dZB (c), and 45 dBZ (d) threshold values from experiments CNTL, CLD, X03 and NoDiv.

thresholds, which reflects the adjustments of initial storms in the first hour of forecast. It can be seen that all scores in the 45 dBZ threshold are better for CNTL than for CLD from a little after 00:00 UTC to 1:00 UTC (Fig. 12d) and all scores are better for CNTL and CLD than for X03 from 00:30 UTC to 1:00 UTC, in agreement with the earlier subjective assessment of the forecast of cell centers. The improvement of CNTL over CLD for 5, 15 and 30 dBZ thresholds are less clear cut during this hour, although the score is generally better at 01:00 UTC, while the score is lower at 00:45 UTC for the other three thresholds. Our subjective analysis does suggest that the forecast of CNTL is superior at 00:45 UTC, however, and the high threshold (45 dBZ) ETS confirms this. The less than clear cut results from the ETS actually suggest that the ETS are not necessary a good measure for evaluating forecasts containing discrete features, for which propagation and phase errors can have a significant impact on the calculated scores. Verification of discrete features remains an active area of research, and our use of the equitable threat score here is only intended to provide some degree of objectivity. The scores for experiment NoDiv will be discussed later.

c. Experiments using radial velocity only and with no radar data

In the previous subsection, we found that radial velocity data, when used (via 3DVAR analysis) together with reflectivity data (via cloud analysis), can give positive impact on the storm forecast. In this subsection, we present results from experiment VR in which cloud analysis with reflectivity data is turned off while radial velocity is assimilated the same way as in control experiment CNTL. The experiment examines the effectiveness of assimilating radial velocity data alone. At the same time, we also present results from another experiment, namely NoVRZ, that does not use any radar data.

The predicted reflectivity fields from experiments NoVRZ and VR mapped to the same elevation scan level are plotted in Fig. 13 at 00:30

UTC March 29, which is in-between the two tornadoes. Compared to the observed reflectivity (Fig. 7e), it can be seen that experiments NoVRZ and VR completely failed to predict storm cells around Fort Worth (Fig. 13). In the forecast of NoVRZ, there are two storm cells to the southwest of Tarrant County (Fig. 13a) and they originated from the 9-km forecast that was used as the background for the initial 3-km analysis at 22:00 UTC. Two storm cells are also found in the forecast of VR, but they show different position and structure (Fig. 13b). In both cases the storms do not match the observed reflectivity, indicating a failure of both forecasts to build and support storm cells in a short-term forecast. Still, some positive impact of assimilating radial velocity data can be found during and shortly after the assimilation cycles. The fields of VR show weak reflectivity centers to the northwest of Fort Worth at the end of assimilation cycles. They decay, however, soon after the forecast period begins (not shown). The results also tell us clearly that assimilating the radial velocity alone via the current 3DVAR procedure is far from enough to create a properly balanced storm in this case. This is not very surprising because the availability of radial velocity data from a single radar, and the lack of strong, reliable link between radial velocity data with other model variables, particularly the buoyancy. More sophisticated equation constraints that better couple together model state variables or flow-dependent background error covariances should help. The former is true with 4DVAR and the latter with the ensemble Kalman filter method. Tong and Xue (2004) found with observing system simulation experiments (OSSE) that radial velocity has more positive impact than reflectivity when assimilated using ensemble Kalman filter method for a simulated supercell storm. Radial velocity also plays a key role in 4DVAR assimilation work such as Sun and Crook (1997).

Based on the above results, we conclude that the assimilation of both radial velocity and reflectivity data from a single Doppler radar via an inexpensive intermittent assimilation procedure is effective to build pre-existing storms in a nonhydrostatic model at 3-km resolution. The analysis procedure employs 3DVAR for the analysis of radial velocity as well as conventional observations, and a diabatic cloud analysis scheme for assimilating reflectivity data. The forecast starting from the assimilated initial condition is able to capture most of the key characteristics of the observed storms for a two-hour period. Although reflectivity data are found to have more positive impact on the storm forecast than radial velocity with the current analysis procedure, the use of radial velocity along with reflectivity do improve the quality of forecast, and more so in terms of the strong low-level vorticity centers associated

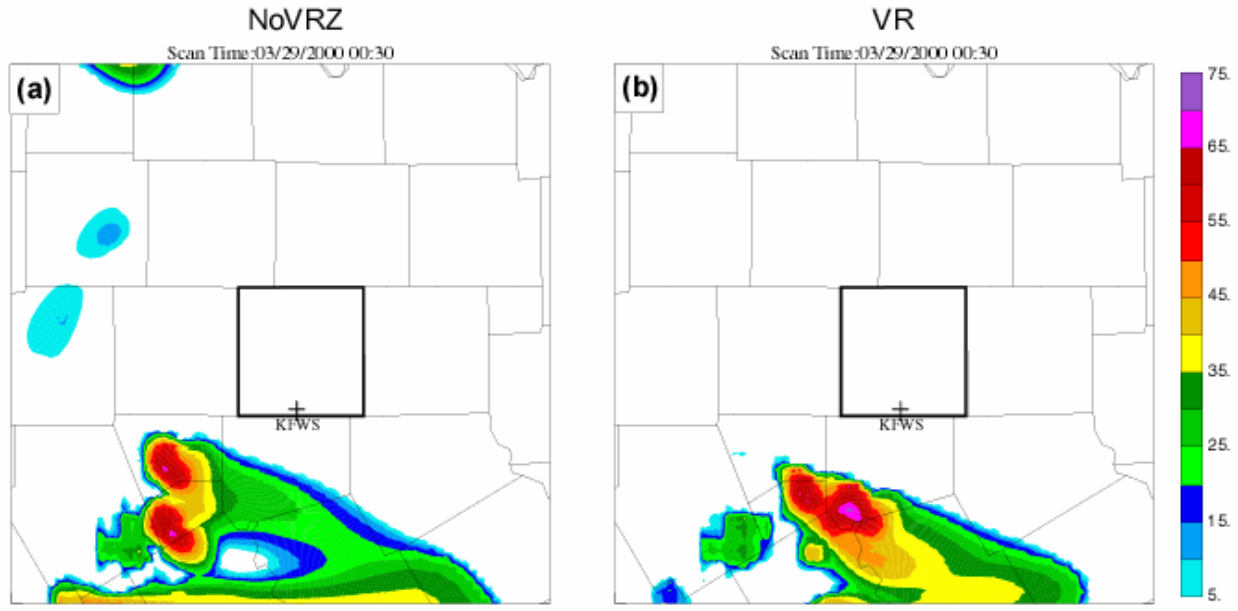

Fig. 13. Similar to Fig. 7, except that they are predicted reflectivity fields from experiments NoVRZ and VR at 00:30 UTC March 29, 2000.

with the expected tornadogenesis. The possible reason is that the initial thermal, moisture and cloud field disturbances introduced by the reflectivity can sustain during forecast and induce corresponding changes in wind field but initial wind disturbances from radial velocity disperse quickly in the form of acoustic waves in the absence of proper balances with other fields and among the three wind components themselves. Next, we will examine various formulations of the mass continuity constraint which may play a role in initializing the proper balance.

d. Experiments on mass continuity constraint

All of the above experiments that assimilate radial velocity data use a two-dimensional mass continuity equation or the horizontal mass divergence as a weak constraint. To better understand the impact of mass continuity constraint, five additional experiments, namely, NoDiv, Div2Da, Div2Db, Div3Da and Div3Db, are conducted. For brevity, we present only results of these experiments at 00:30 UTC March 29, corresponding to 1.5 hour forecast time. The predicted reflectivity mapped to the same 1.45° radar elevation level of KFWS radar is plotted in Fig. 14 for CNTL and the above five experiments. The corresponding surface and 3 km MSL wind and vorticity fields are plotted in Fig. 15. The ETS for reflectivity for these experiments are plotted Fig. 16 and Fig. 17, together with that for CNTL. The ETS for NoDiv are also plotted in Fig. 12 for easier comparison with those of CNTL and CLD.

Experiment NoDiv in which mass continuity constraint is not imposed at all in 3DVAR radial velocity analysis is designed to separate effect of mass continuity from that of radial velocity. Comparing Fig. 14b with the corresponding observation in Fig. 7e, it is seen that Storm A is over predicted by NoDiv in size and its location is biased southward while Storm B is completed missed. Storm D is located too far to the east, by almost one county, and it is trailed by a spurious, though weaker, cell to its west. Another spurious cell, labeled D' in the figure, is found to the north-northeast of cell D. It is labeled D' because it is a cell that split from Storm D in the first half hour of forecast (not shown). As shown in Fig. 14a for this time and discussed in detail for other times earlier, the forecast of CNTL is clearly more accurate than that of NoDiv. The ETS of NoDiv for the 45dBZ threshold are lower than both CNTL and CLD during the important period between 00:00 and 1:00UTC (Fig. 12d).

The above comparisons demonstrate the importance of including mass continuity constraint when analyzing radial velocity data. This is because, as discussed earlier, a single Doppler radar observes wind along the radial direction only. The cross-beam components cannot be determined by the 3DVAR analysis, without additional information that links the three components. Without any constraint, 3DVAR tends to make adjustment of background winds along the radial direction only, leaving the other components essentially unchanged. The inclusion of a 3D anelastic mass-continuity constraint at least forces the other wind components to respond to changes along the radial direction and to produce an analysis that more or less satisfy the mass continuity equation. The problem related to the finite difference implementation of this constraint in the case of large grid aspect ratio is another issue.

Without the mass continuity constraint, large amplitude acoustic oscillations are found in the time series plots of surface pressure in NoDiv (not shown). Imposing physic laws, here the mass continuity, helps control the noise by producing a more physically consistent wind analysis. Treating the constraint as a week constraint gives the system necessary flexibilities which is discussed for dual-Doppler analysis by Gao et al (1999). In the case of dual-Doppler wind analysis, two of the three wind components can be determined while the mass-continuity equation gives the third, yielding an easier problem than we have here.

The sensitivity of storm forecast on weighting coefficient λ_c of mass continuity constraint in the cost function is studied through experiments Div2Da and Div2Db in which λ_c is half or double the value of CNTL (Table 1), respectively. In the 1.5-hour forecasts of these three experiments (Fig. 14a, c, d), the storms show a similar general pattern with several differences in the fine structures. First, Storms A and B in experiment Div2Db are not separate as in the other two experiments and in the real world. Second, the maximum reflectivity center of Storm A in Div2Db has greater displacement errors. Third, Storm D in Div2Da and Div2Db has a greater eastward displacement error than in CNTL. Although the pattern comparison shows that the forecast of experiment CNTL is somewhat better than that of Div2Da and Div2Db at this time, the latter achieved generally better ETS (Fig. 16). For the 45 dBZ threshold, Div2Db outperforms the other

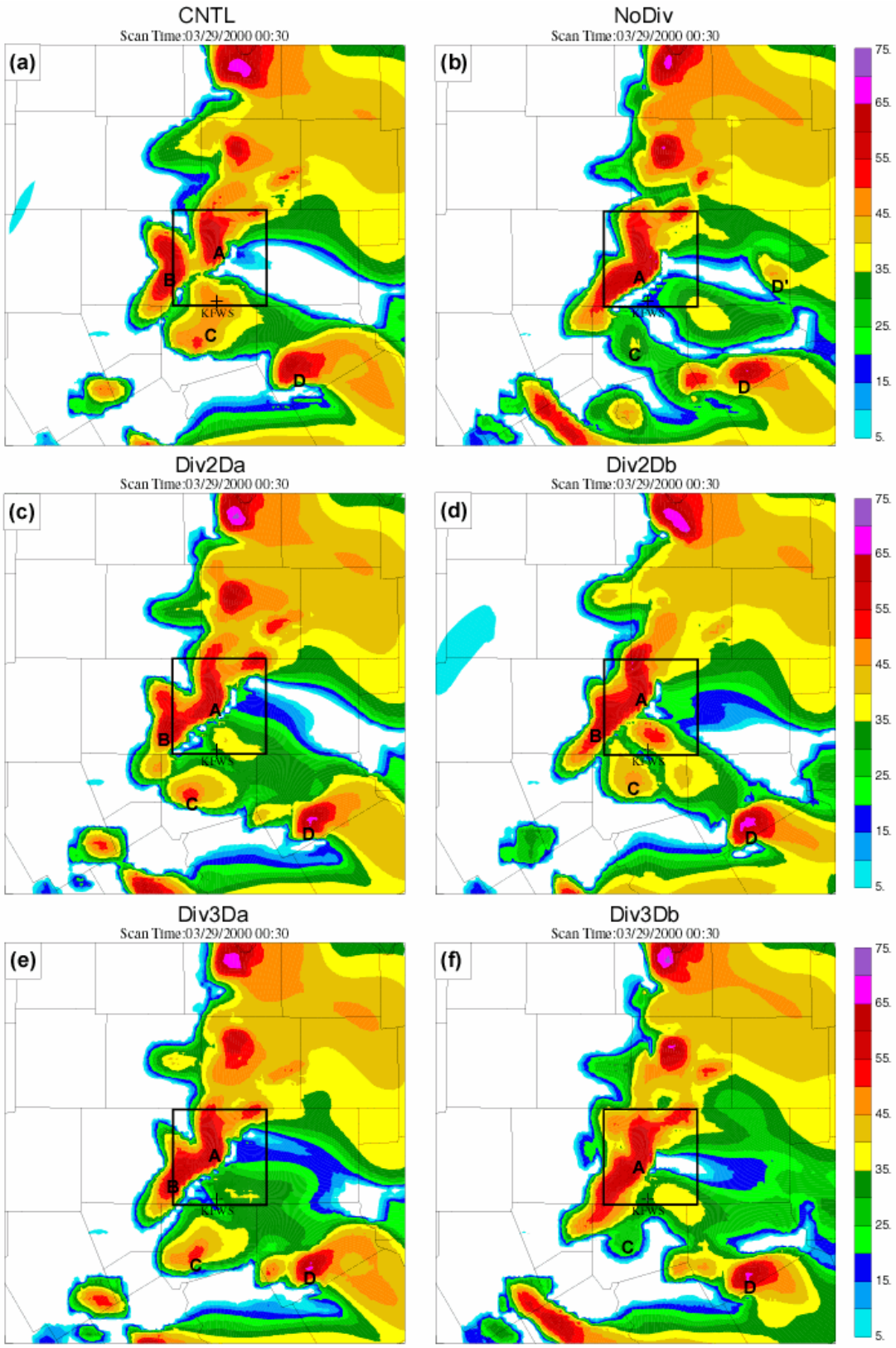

Fig. 14. Similar to Fig. 7, except that they are predicted reflectivity fields from experiments CNTL (a), NoDiv (b), Div2Da (c), Div2Db (d), Div3Da (e) and Div3Db (f), at 00:30 UTC March 29, 2000.

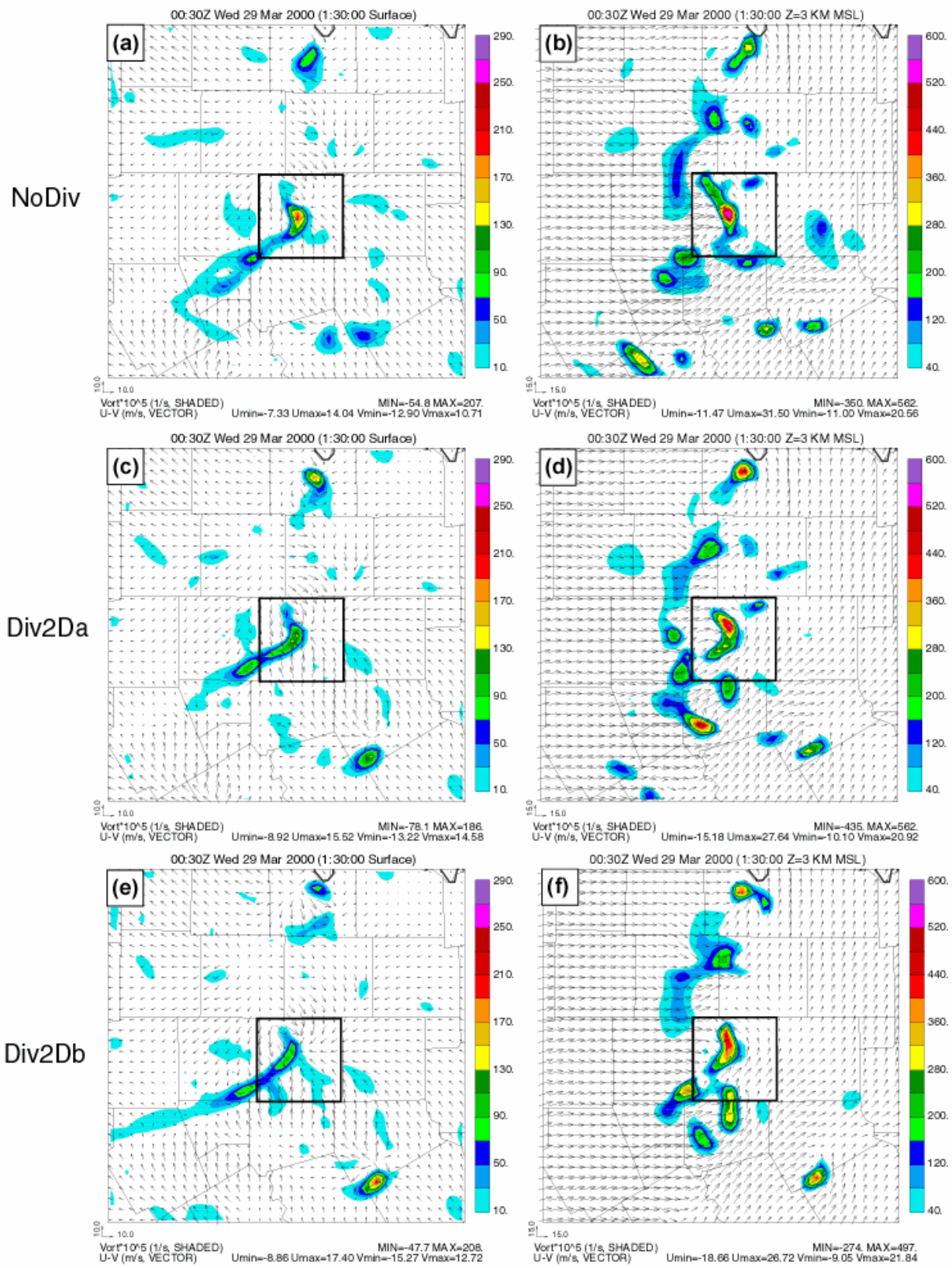

Fig. 15. Similar to Fig. 8, except that they are predicted wind and vorticity fields from experiments NoDiv, Div2Da, Div2Db, Div3Da and Div3Db at 00:30 UTC March 29, 2000.

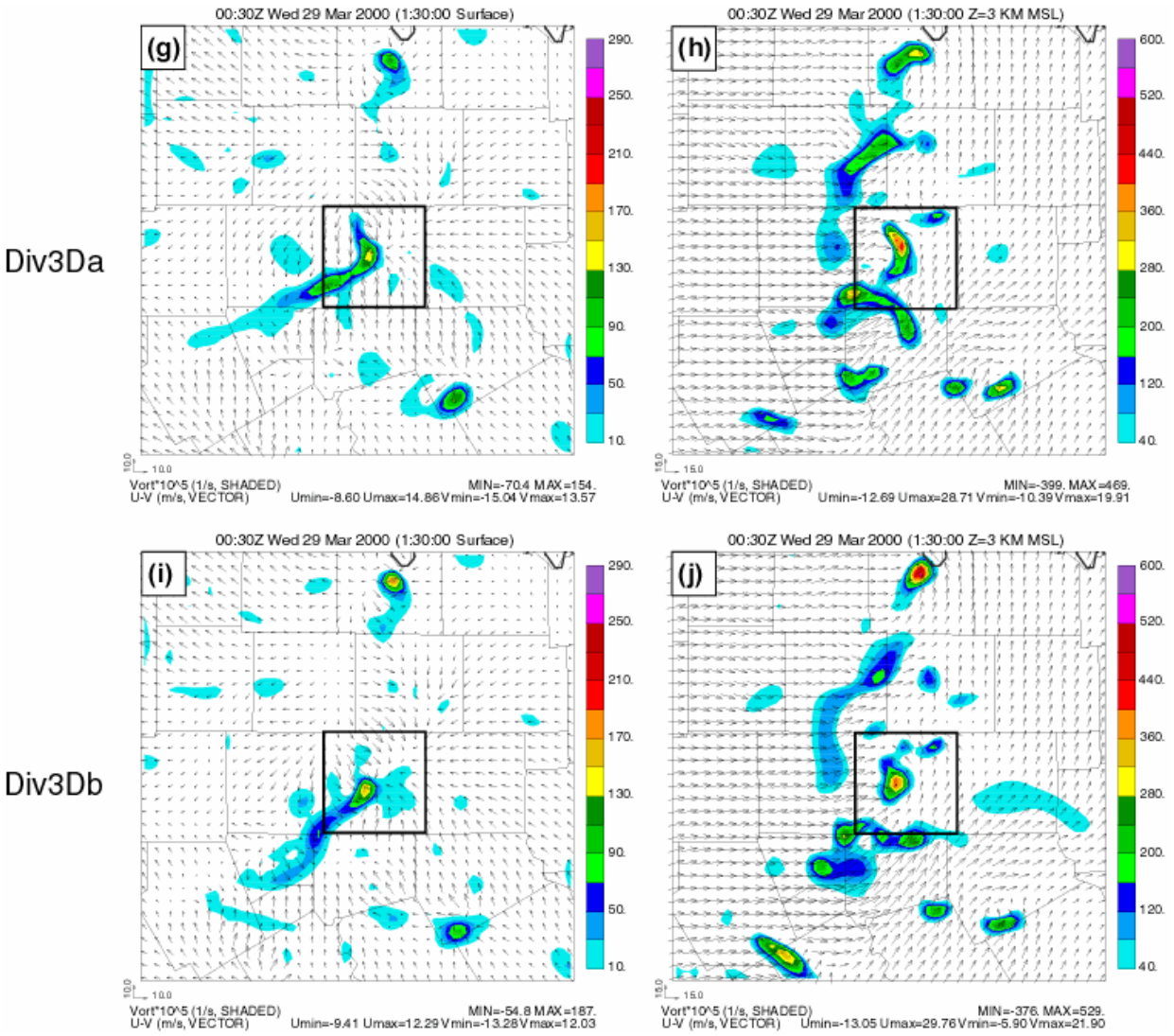

Fig. 15. Continued.

two at 00:30 UTC, but overall, the scores of the three are similar, especially considering such equitable threat scores are not necessarily complete measures of the true forecast quality. In general, it appears that the analysis and forecast are not very sensitive to the coefficient of the continuity constraint for this case.

In section 2c, we illustrated the problem with using a 3D mass continuity constraint on a grid with large aspect ratios (between horizontal and vertical grid intervals). In such a situation, the vertical part of the mass divergence dominates the wind adjustment so that horizontal wind components are little adjusted. This is the main reason why a 2D mass divergence constraint is used in all the earlier experiments. It should be pointed out, however, the 2D mass-divergence constraint is not really physical for convective scale flows, which can exhibit significant horizontal divergence beneath strong updrafts. To study this problem further, two experiments employing 3D mass continuity constraint are performed. Experiment Div3Da uses different weighting coefficients for the horizontal and vertical parts of the 3D mass continuity constraint while experiment Div3Db uses the same weighting coefficient for both parts, which is effectively a true 3D mass continuity constraint. The exact vales of the weighting coefficients are listed in Table 1.

As we expected, experiment Div3Db gives very similar forecast for main storm cells at 00:30 UTC as experiment NoDiv (Fig. 14b, f) because almost all wind adjustment were applied to the vertical velocity, and the adjustment is expected

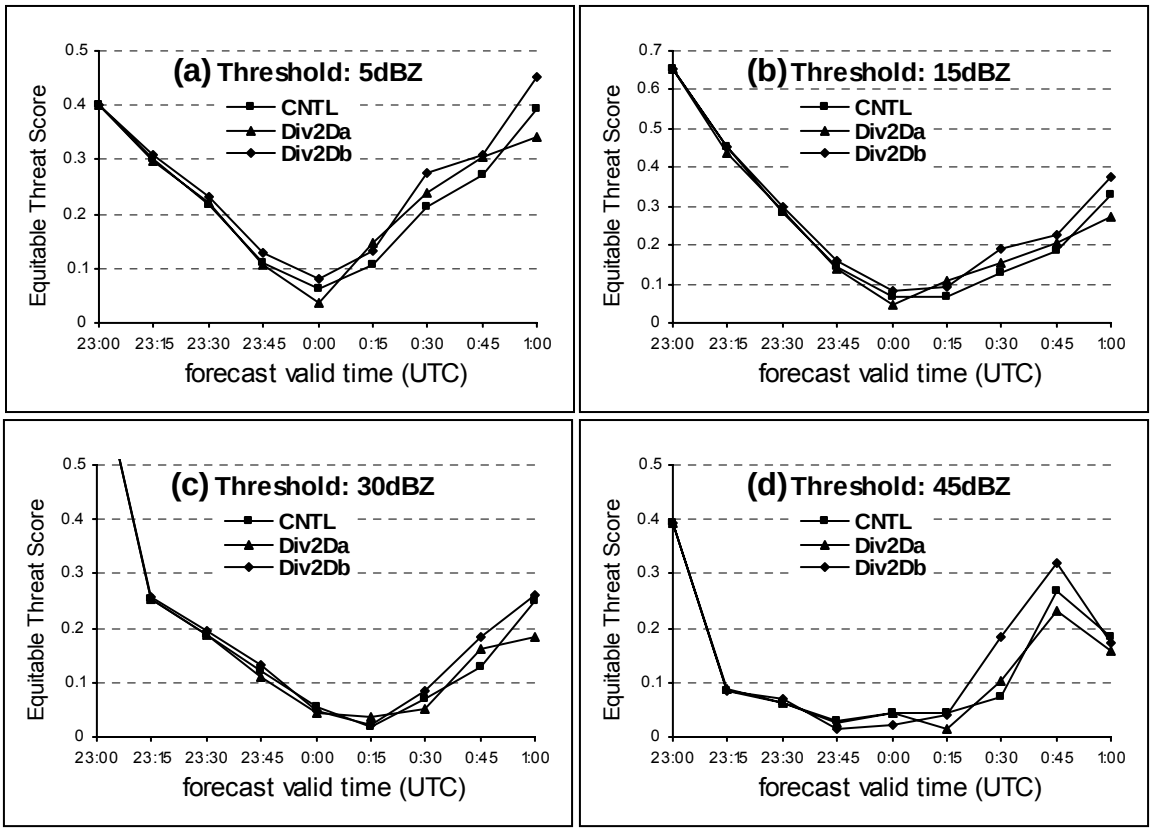

Fig. 16 Same as Fig. 12 but for experiments CNTL, Div2Da and Div2Db.

to be one orders of magnitude smaller (because of large aspect ratio) than those of horizontal winds for the 3D mass continuity to be satisfied. The ETS of Div3Db and NoDiv shown in Fig. 17 are also similar for most of the times and threshold values, suggesting little impact of the 3D mass continuity constraint when the weighting coefficients for horizontal and vertical divergence are the same.

Experiment Div3Da decreases the weighting coefficient for the vertical divergence by a factor of ten compared to CNTL or the horizontal term in Div3Da. Doing so decreases the effect of vertical velocity adjustment thereby giving greater adjustments to the horizontal winds. The forecast reflectivity field plotted for Div3Da in Fig. 14 looks similar to that of Div2Db, and is better than that of Div3Db, indicating the increased role of adjustments to horizontal wind fields. The ETS of experiment Div3Da for the 45dBZ threshold are in-between those of experiments CNTL and NoDiv (Fig. 17d).

The surface and 3 km MSL wind and vorticity fields from the above five experiments, (i.e., NoDiv, Div2Da, Div2Db, Div3Da and Div3Db) are plotted in Fig. 15 and they can be compared to the corresponding times of CNTL in Fig. 8. Interestingly, all five experiments predicted a well-defined, column of high vorticity over Fort Worth just as in experiment CNTL, but their shape and intensity differ somewhat. However, considering the fact that the forecast with no radial winds (experiment CLD) failed to produce this high vorticity column, we can credit the radial velocity for the formation of this mesocyclone.

In summary, we found in this section that the proper inclusion of a mass continuity or divergence constraint in the 3DVAR analysis increases the positive impact of radial velocity data on the thunderstorm analysis and forecast in our case, but for the predicted wind field, the differences among the divergence constraints is much less than the impact of adding winds by any method. Due to the large grid aspect ratios, especially at the low levels for a vertically stretched grid, a constraint that limits the magnitude of horizontal mass divergence or a 3D formulation with a much smaller coefficient for the vertical component is found to work most effectively.

e. Sensitivity to details of cloud analysis

To identify the impact of each modification in cloud scheme on the results of assimilation and forecast, three experiments are done: 1) CTLH, in which in-cloud temperature adjustment is based on latent heat conversion instead of moist adiabatic temperature profile, 2) CMAX for which the quantities of the precipitation species are determined by the maximum value of background and retrieval instead of the observation-based retrieval values alone, and 3) CKRY, which uses the KRY scheme instead of the SMO scheme to retrieve the quantity of each precipitation species. All other options in these experiments are the same as CLD. Comparison among these experiments will give us some insight on the effect of the new cloud analysis procedure.

1) Results of assimilation

In above study, it is found that information on the storm-scale is largely added to the system via the cloud analysis in the data assimilation cycles. Modifications to the cloud analysis will directly influence results of the assimilation and the ensuing model forecast.

Reflectivity fields from the assimilation output of the five experiments in table 2 mapped to the elevation 1.45° scan of radar KFWS are plotted in Fig. 18 along with the corresponding observed radar echoes. In the initial field of CLD, the storm structures look very much like the observed reflectivity, though the interpolation scheme and cloud processing make the features smoother than the observed ones (Fig. 18a, b). Keeping in mind that CLD uses the retrieved quantity of the precipitation species directly in the analysis, it is fully expected that the assimilation reflectivity and observation match each other very well. In contrast, the initial reflectivity field in X03 only gives the basic structure of storm cluster and loses many details of storm cells (Fig. 18c). Experiment CTLH has the identical initial reflectivity field to

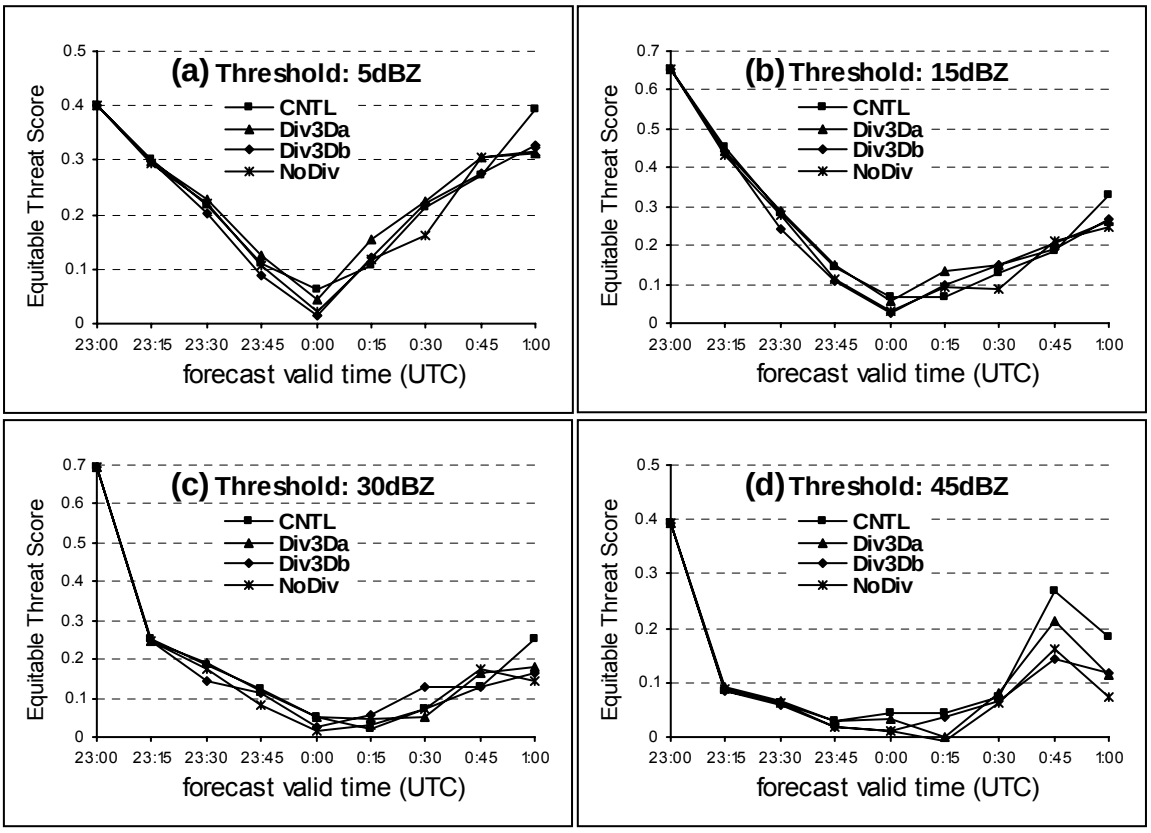

Fig. 17. Same as Fig. 12 but for experiments CNTL, Div3Da, Div3Db, and NoDiv.

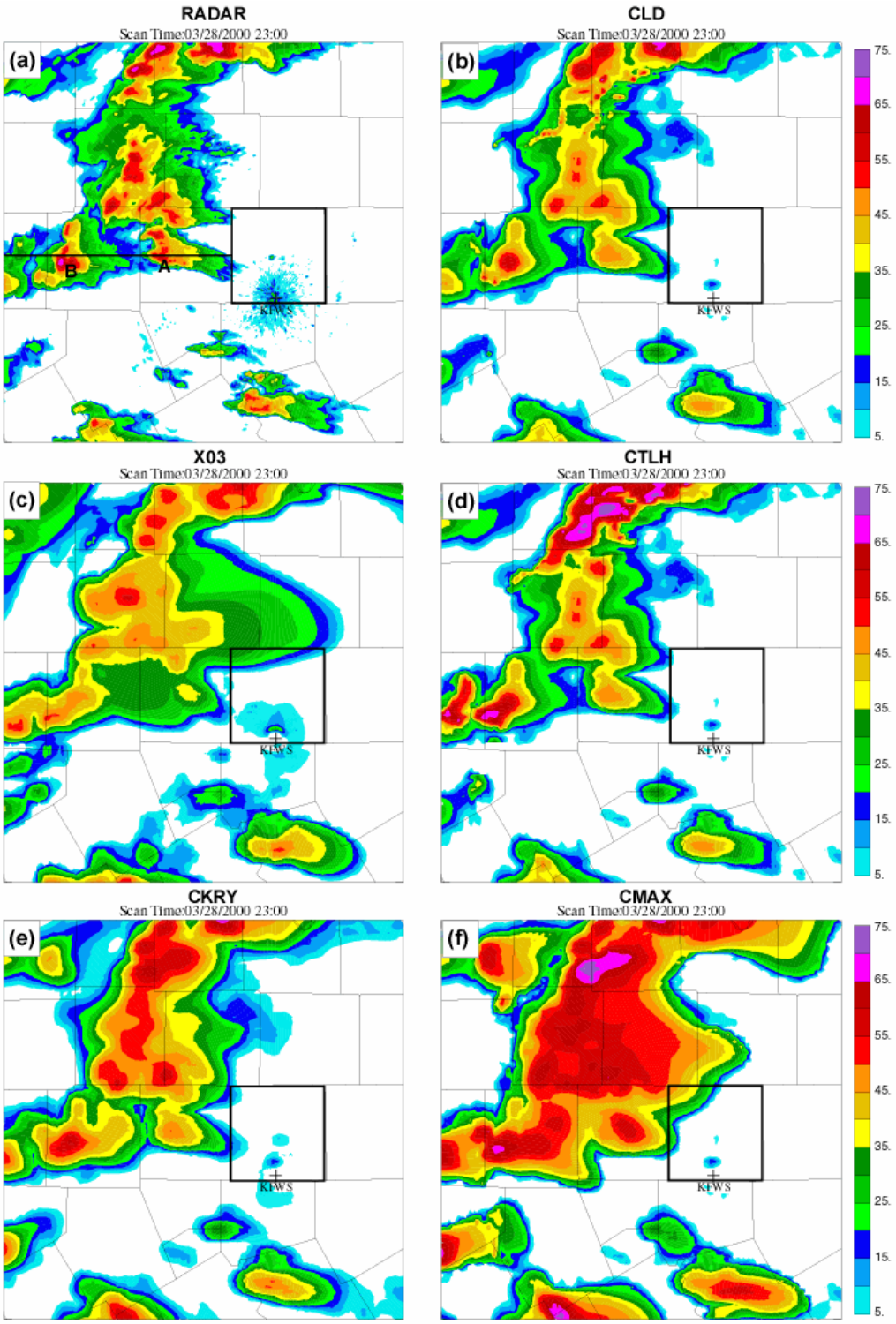

Fig. 18. Reflectivity fields at 1.45° elevation scan of KFWS from assimilation results of experiments CNLY(b), X03(c), CTLH(d), CKRY(e), and CMAX(f) and corresponding radar observation(a). Major storm cells are marked by capital letters in (a). Tarrant County is highlighted and about 50×50 km2 in size. The domain shown is about 200 km on each side, representing the portion of 3 km grid between 70 and 270 km in east-west direction and from 60 to 260 km in north-south direction.

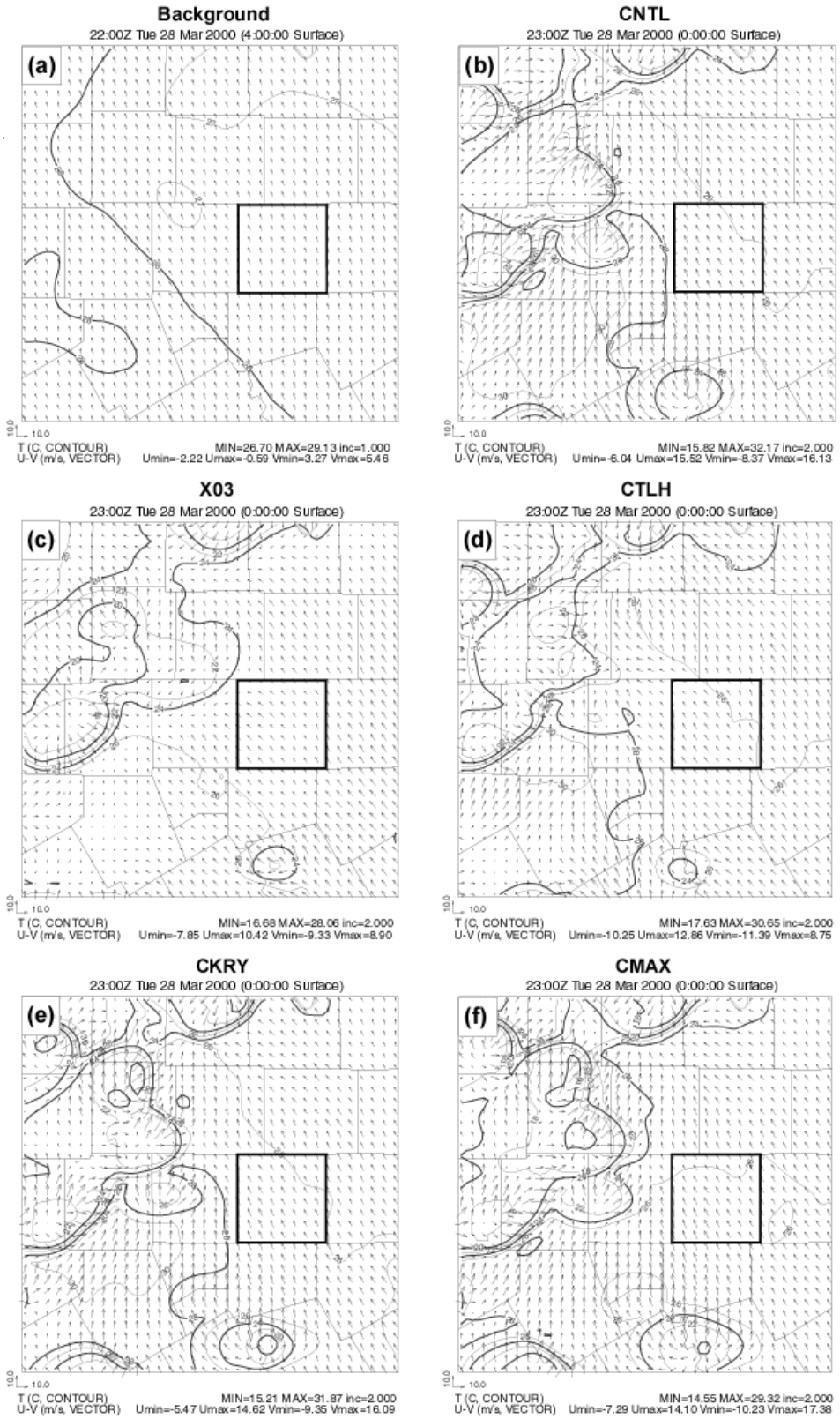

Fig. 19. Surface wind and temperature fields from assimilation results of experiments CNLY(b), X03(c), CTLH(d), CKRY(e), and CMAX(f) and background(a). The domains shown are the same as in Fig. 18.

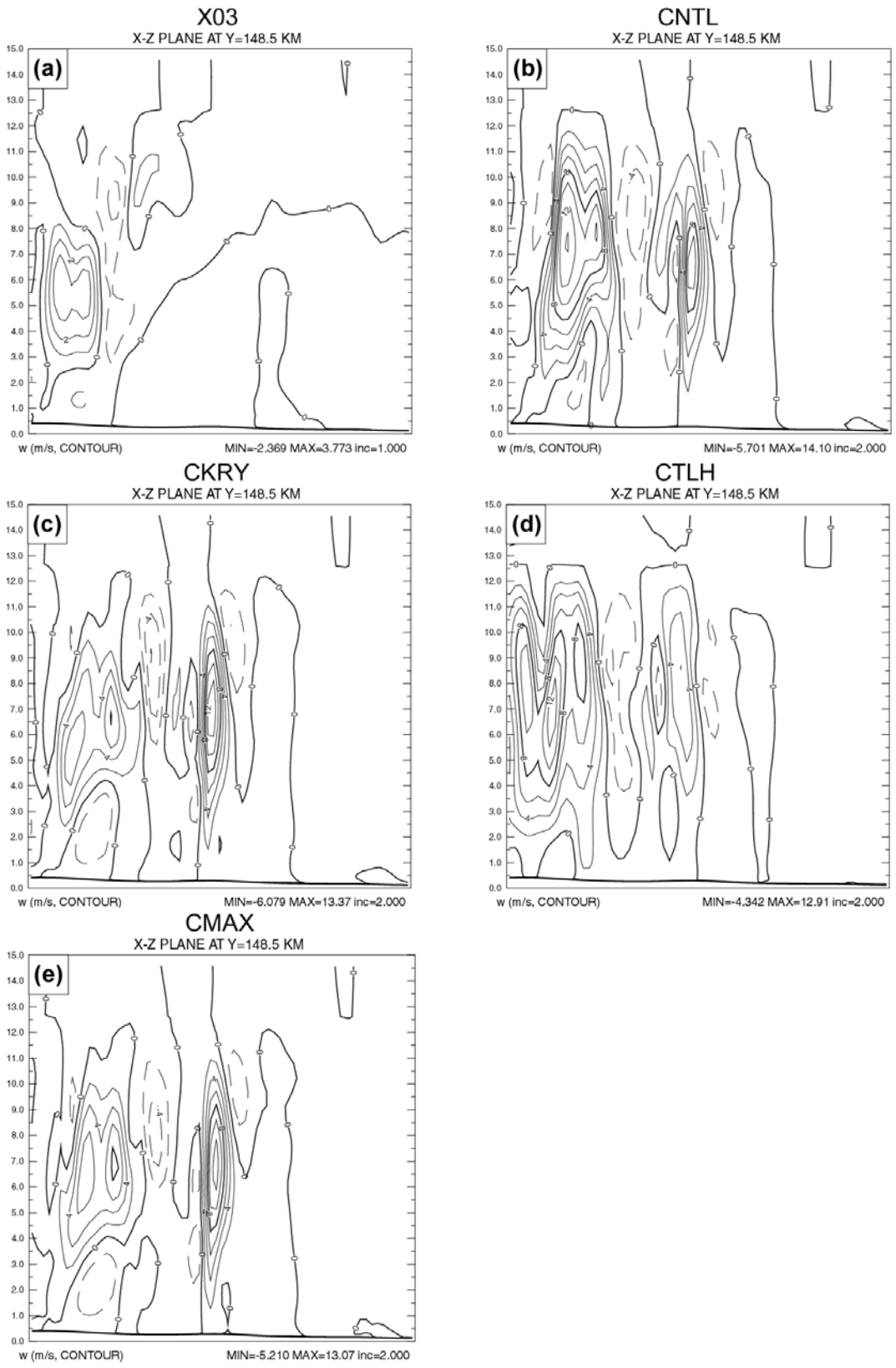

Fig. 20. Cross section (along line in Fig. 19a) of vertical velocity fields from assimilation results of experiments X03(a), CNLY(b), CKRY(c), CTLH(d), and CMAX(e).

that of CLD in the area near the radar (Fig. 18d), but has stronger reflectivity maxima than their counterparts in CLD in the area distant from the radar because the two experiments have different mid-level temperature fields as depicted in Section 3c. Experiment CKRY uses simple radar reflectivity equations to retrieve precipitation species, so its result is a little smoother than that of CLD (Fig. 18e). From the initial reflectivity field of CMAX, the influence of the background values of the precipitation species can be seen clearly in Fig. 18f because in this case the maximum value of background and retrieved precipitation species is used for the analysis values, and the background reflectivity is generally greater than the observations at this time through much of the domain.

The surface wind and temperature fields from all five experiments in table 2 and from the background before 3 km analysis are plotted in Fig. 19. In this figure the storm-related gust fronts and cold pools are found in the initial fields of all five experiments. As was noted in the forecasts of reflectivity, the CLD run (Fig. 19b) induces more details of storms in its initial field than X03 (Fig. 19c). In the initial surface wind and temperature fields from CTLH, CKRY, and CMAX (Fig. 19d, e, f), only CTLH has large differences from CLD; its appearance is more like X03. Both CTLH and X03 underestimate the strength of the cold pool and gust front related to Storm A (Fig. 18a). That indicates the formation of cold pool and gust front is very sensitive to the choice of temperature adjustment scheme, presumably through the direct effect of the latter on storm intensity.

The strength of the updraft is an important indicator for the vigor of a thunderstorm. Fig. 20 is the cross section of vertical velocity, w, fields along a line through Storms A and B (Fig. 18a). In X03, the updraft related to Storm B is weak and there is no sign of the existence of Storm A (Fig. 20a) in this cross-section, while in CLD (Fig. 20b), two large updraft centers associated with Storms A and B are found. It shows that storms have been built up through assimilating Level-II reflectivity data by the new cloud analysis procedure. The vertical velocity fields from CMAX, CKRY and CTLH reflect varied impacts of each modification (Fig. 20c, d, e). Each of them has just one strong updraft center and one weak updraft center in the initial w field. Comparing Fig. 20 to the corresponding surface wind and temperature fields (Fig. 19), it is found that the vertical motion of Storm A is strongly related to the strength of its the surface cold pool and gust front.

2) Results of forecast

In the above subsection, we have seen that assimilation results are obviously affected by modifications to the cloud analysis procedure. In this subsection, forecasts initialized from the results of assimilation are compared so as to make further inferences on the effects of these modifications. Fig. 21 shows the predicted reflectivity mapped to the 1.45° elevation level of KFWS radar from CTLH, CMAX, and CKRY at the time of the tornadoes. The surface wind and temperature fields from the same experiments and times are plotted in Fig. 22.

Since CMAX, CKRY and CTLH each has only one aspect in their cloud analysis procedure that is different from that of CLD, the main characteristics of their predicted storm cluster are similar to that of CLD at the time of the downtown Fort Worth tornado (Fig. 21a, c, e, Fig. 9d). Focusing on the details of Storm A, it is found that Storm A in CKRY and CTLH has the same shape and position as in CLD, while the storm moves a little faster in CMAX than in CLD. The gust fronts related Storm A tell the same story as the reflectivity fields. That is, the gust fronts of Storm A in CKRY, CTLH, and CLD (Fig. 10b, Fig. 22c, e) are in similar positions, while that in CMAX moves faster (Fig. 22a) than that in the other experiments. All three experiments have spurious Storms A' and D' appearing in the forecast at this time (Fig. 21a, c, e).

By 00:45 UTC, the differences among CMAX, CKRY, CTLH and CLD have increased (Fig. 21b, d, f, and Fig. 9h). Storm A in CMAX has obviously led its counterpart in CLD and connected with spurious Storm D'. It will propagate into the center of Dallas County in next 15 minutes of the forecast as Storm A does in X03. The northern part of its gust front in CMAX has reached the east boundary of Tarrant County and the southern part is approaching to the southeast corner of the county (Fig. 22b). Although Storm A in CKRY and CTLH has the same position at 00:15 UTC, it propagates in different directions in these two experiments during the following half an hour. In CKRY, Storm A moves southeast to the center of Tarrant County and lags Storm A in Experiment CLD. In Experiment CTLH, Storm A goes northeast and has run out of Tarrant County from its northeast corner. In surface wind and temperature fields of CKRY and CTLH (Fig. 22d, f), the cold pool and gust front of Storm A follow the same motion direction and reach the same position as the reflectivity.

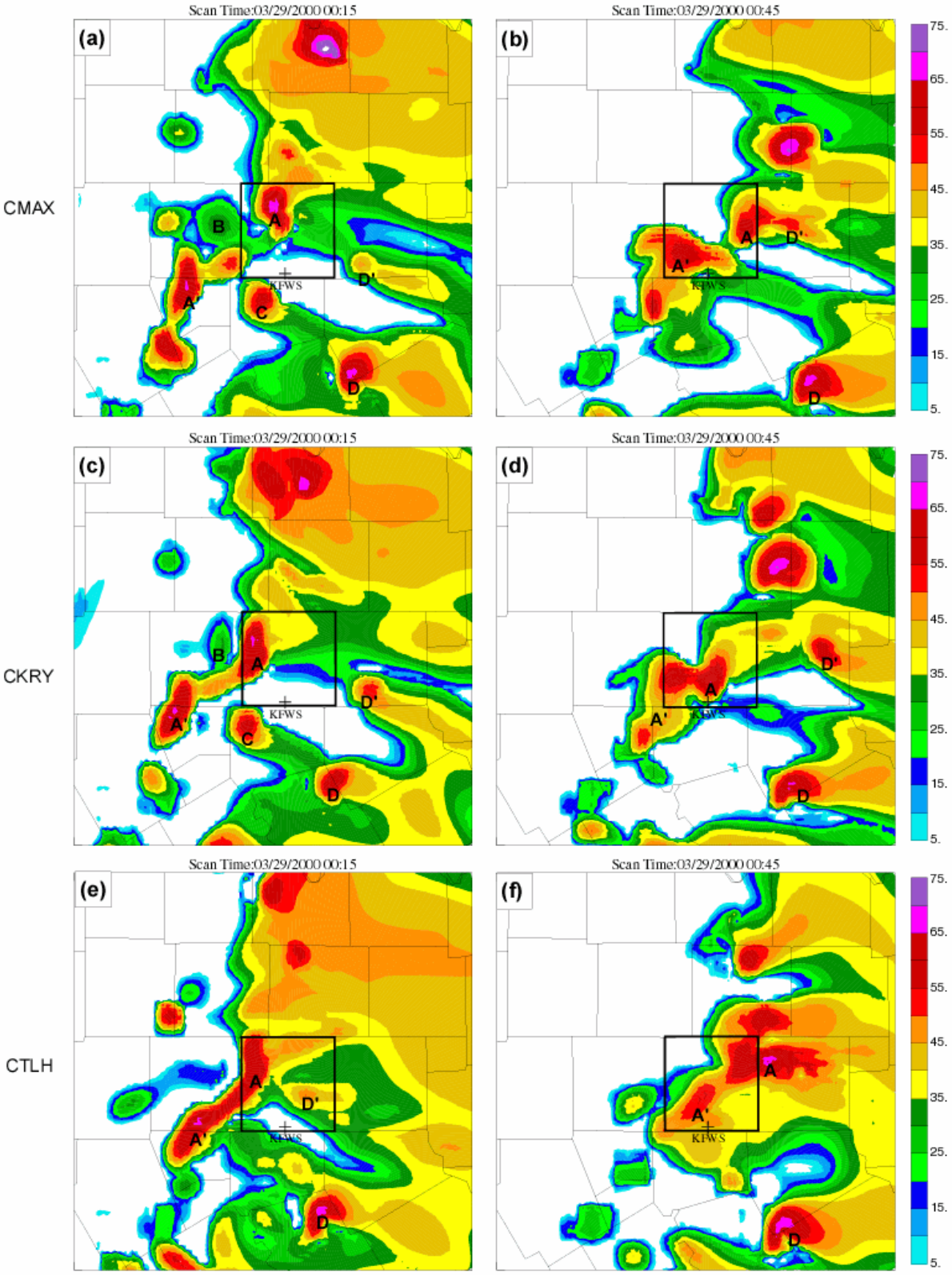

Fig. 21. Similar to Fig. 7, except that they are predicted reflectivity from experiments CMAX, CKRY and CTLH at 00:15 UTC and 00:45 UTC March 29, 2000.

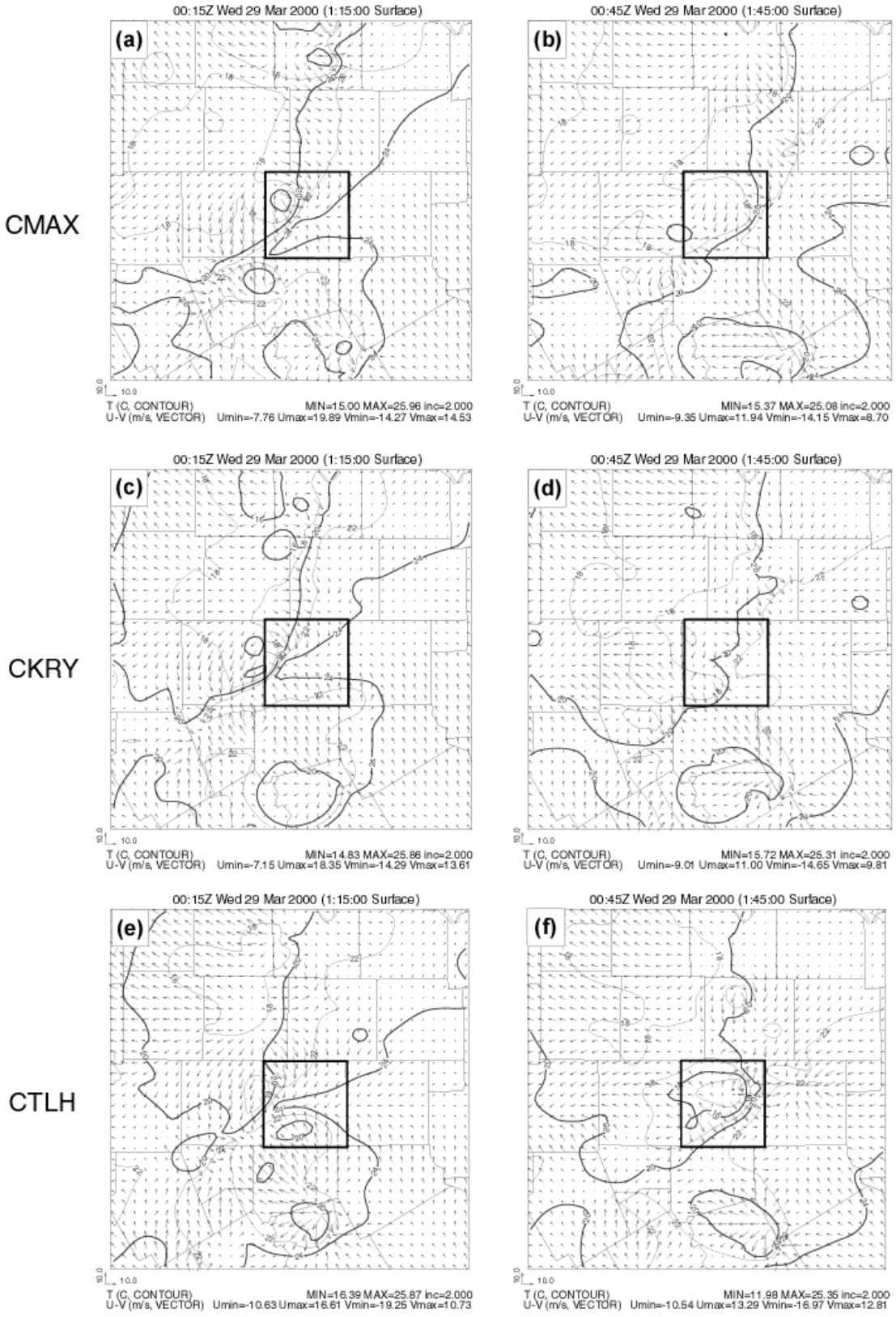

Fig. 22. Similar to Fig. 10, except that they are from experiments CMAX, CKRY and CTLH at 00:15 UTC and 00:45 UTC March 29, 2000.

Another big difference among these experiments at 00:45 UTC is the behavior of spurious Storm D'. It remains as a strong isolated echo in CKRY (Fig. 21d), connects with Storm A in CMAX (Fig. 21b), and has merged into Storm A in CTLH (Fig. 21f) and partly account for the fast motion of Storm A in that experiment. The spurious Storm D' does not exist after 00:15 UTC in the forecast of CLD (Fig. 9), while it merges with Storm A at 00:30 UTC in the forecast of experiment X03 and causes large location errors of Storm A at 00:45 UTC.

The comparisons above show that adjusting in-cloud temperature based on moist adiabatic profile and choosing retrieved precipitation species as analysis value in new cloud analysis procedure slow down the motion of predicted tornadic Storm A during the period of the tornado occurrence. These two modifications, together with the use of SMO scheme to retrieve precipitation species, contribute to the erasure of spurious Storm D' and then further avoid the erroneous acceleration of Storm A found in the X03 forecast. So the CLD with all the modifications of the new cloud analysis procedure gives the best forecast for the tornadic thunderstorm during the critical tornado outbreak period in this case.

6. SUMMARY AND DISCUSSION

In this paper, the impact of Level-II WSR-88D radial velocity data and the new cloud analysis procedure with the WSR-88D Level II reflectivity data on the prediction of a cluster of tornadic thunderstorms is studied. The March 28, 2000 Fort Worth tornado outbreak observed by the Fort Worth (KFWS) WSR-88D radar is used as a test case and compared to the results of Xue et al (2003). A 3-km resolution grid nested inside a 9-km one is used for both assimilation and prediction experiments. For most 3-km experiments, a one-hour long assimilation with analysis cycles at 10-minute intervals is performed, which is followed by a three-hour forecast starting from the assimilated initial condition. Radial velocity data are used in 3DVAR analysis that contains a mass continuity constraint in the cost function and reflectivity data are assimilated through a complex cloud analysis procedure.

Results from nine 3-km experiments in table 1 are discussed which examine the use and impact of Level II radial velocity data from KFWS radar. Four more 3km experiments in table 2 are conducted to investigate the impact of three modifications to the cloud analysis procedure on the forecast of thunderstorms. The results in the paper demonstrate that the ARPS 3DVAR is capable of successfully analyzing observations from different sources, including those from radiosonde (available at 18 UTC), surface stations and Doppler radars. Combined with intermittent assimilation cycles, positive impact of radial velocity data and new cloud analysis scheme is obtained for the forecast of a cluster of thunderstorms.

The best prediction is obtained when both reflectivity and radial velocity data are assimilated. The prediction is able to match up individual storm cells on the 3 km grid up to two hours into the prediction, and the supercell characteristics of the storm that spawned two individual tornadoes are well predicted, with timing errors of less than 15 minutes, and location errors of less than 10 km at the time of the tornado outbreaks.

Starting from an initial condition which assimilates Level-II reflectivity data through the new cloud analysis procedure, the experiment CLD successfully reproduces the evolution of the most significant thunderstorms in the Fort Worth tornado case. The forecast shows a storm with high reflectivity, strong gradients in reflectivity, and a gust front with areas of strong convergence approaches and passes through downtown Fort Worth and Arlington around the time of the tornado occurrences. Comparing to an earlier experiment, X03, that used an earlier version of the cloud analysis with Level-III reflectivity data in the assimilation cycles, the experiment with all the recent modifications to the cloud analysis, CLD, shows reductions in both timing and location errors for the main tornadic thunderstorm.

The comparison of data denial experiments show that reflectivity data has a greater positive impact on the storm forecast than radial velocity using the current 3DVAR and cloud analysis procedure, while the use of radial velocity along with the reflectivity via cloud analysis does incrementally improve the storm forecast, especially in terms of the strong low-level vorticity centers associated with the tornadogenesis. When no radar data or radial velocity only (in addition to conventional data) is used, the model fails to forecast nearly all storms around Fort Worth. The small impact of using radial velocity alone is related to the limitation of the current 3DVAR wind analysis procedure which does not make use of radar scans at multiple times and uses only a simple mass continuity equation constraint that does not solve the under-determinedness problem for single-Doppler wind analysis. Specifically the lack of introduction of buoyancy in the clouds hurts the

forecast. The current cloud analysis is effective in sustaining storms in the model forecast, however.

It is also found through a separate set of experiment that the correct use of a mass continuity constraint in the 3DVAR analysis can maximize the impact of radial velocity data on the forecast of storms in terms of reflectivity field, but the effect of different formulations of the constraint has a weaker impact on the forecasted wind fields.

The analysis shows that the storm status in the initial field and the evolution of the storm in the forecast can be affected by each individual modification in the cloud analysis scheme. It is found that adjusting in-cloud temperature based on a moist adiabatic profile and choosing retrieved quantities of the precipitation species over background values in cloud analysis can slow the movement of storms in this case and improve the forecast for the tornadic storm. These two modifications, and the use of the SMO scheme to retrieve precipitation species, work together to prevent spurious Storm D' from appearing in the forecast.

Adding hydrometers and adjusting the in-cloud temperature and moisture field in the model initial fields are expected to reduce the spin-up problem in the forecast. From the experiments in this study, the forecast storms still have an adjustment period when the model forecast begins using an initial field from the current cloud analysis procedure. This indicates that there still exist some inconsistencies between the cloud analysis and the model microphysics and cloud dynamics. Some of the adjustment may be handled by use of the existing incremental analysis updating procedure (IAU) in ARPS in a 5-10 minute pre-forecast application of IAU. More investigation on the nature of this adjustment are needed to further improve the cloud analysis procedure.

Still, the rather good forecast of the tornadic thunderstorm in the control experiment shows that a high-resolution model like ARPS together with an adequate system that assimilates WSR-88D Level II data is able to initialize pre-existing thunderstorms and predict them with reasonable accuracy on the cell by cell basis for up to 2 to 3 hours. The 3-km resolution used here is reachable operationally in the near future, over larger domains. Our conclusions are, however, based on only one case. We have collected data for several other severe weather outbreaks and will simulate them with the same assimilation and forecast system to investigate the issues of this paper further. A recent study of Dawson and Xue (2004) on the impact of mesoscale data and cloud analysis on the forecast of a pre-existing mesoscale-convective system (MCS) finds significant positive impact of cloud analysis that lasts as long as 12 hours, although in that case, the MCS still forms in the model even with interpolated Eta analysis, but with significant time delay.

Acknowledgments. This work was supported by a DOT-FAA grant NA17RJ1227, and by NSF grants ATM-9909007, ATM0129892, ATM-0331594, ATM-0331756 and EEC-0313747. The second (MX) was also supported by a grant from Chinese Natural Science Foundation No. 40028504. Drs. Alan Shapiro, and Bill Martin are thanked for very helpful discussions. ZXPLOT was used for the graphics. Supercomputers at OSCER, University of Oklahoma were used for most of the experiments.

7. REFERENCES

Albers, S. C., J. A. McGinley, D. A. Birkenheuer, and J. R. Smart, 1996: The local analysis and prediction system (LAPS): Analysis of clouds, precipitation and temperature. *Wea. Forecasting*, **11,** 273-287.

Bratseth, A. M., 1986: Statistical interpolation by means of successive corrections. *Tellus*, **38A,** 439-447.

Brewster, K., 1996: Application of a Bratseth analysis scheme including Doppler radar data. *Preprints, 15th Conf. Wea. Anal. Forecasting*, Norfolk, VA, Amer. Meteor. Soc., 92-95.

—, 2002: Recent advances in the diabatic initialization of a non-hydrostatic numerical model. P*reprints, 15th Conf on Numerical Weather Prediction and 21st Conf on Severe Local Storms,* San Antonio, TX, Amer. Meteor. Soc., J6.3.

Crum, T. D. and R. L. Alberty, 1993: The WSR-88D and the WSR-88D operational support facility. B*ull. Amer. Meteor. Soc.,* 7**4,** 1669-1687.

Davies-Jones, R., R. J. Trapp, and H. B. Bluestein, 2001: Tornadoes and tornadic storms. Severe Convective Storms, I. C*harles A. Doswell, Ed., Amer. Meteor. Soc.,* 167-221.

Dawson, D. T., II and M. Xue, 2004: Numerical forecasts of the 15-16 June 2002 Southern Plains severe MCS: Impact of mesoscale data and cloud analysis. M*on. Wea. Rev., Submitted.*

Droegemeier, K. K., 1990: Toward a science of storm-scale prediction. P*reprint, 16th conf. on Severe Local Storms,* Kananaskis Park,

Alberta, Canada, Amer. Meteor. Soc., 256-262.

—, 1997: The numerical prediction of thunderstorms: Challenges, potential benefits, and results from real time operational tests. WMO *Bulletin,* 46**, 3**24-336.

Ferrier, B. S., 1994: A double-moment multiple-phase four-class bulk ice scheme. Part I: Description. J. *Atmos. Sci.,* 51**, 2**49-280.

Gal-Chen, T., 1978: A method for the initialization of the anelastic equations: Implications for matching models with observations. Mo*n. Wea. Rev.,* 10**6, 5**87-606.

Gao, J., M. Xue, K. Brewster, F. Carr, and K. K. Droegemeier, 2002: New Development of a 3DVAR system for a nonhydrostatic NWP modeol. Pr*eprint, 15th Conf. Num. Wea. Pred. and 19th Conf. Wea. Aanl. Forecasting,* San Antonio, TX, Amer. Meteor. Soc.

Gao, J.-D., M. Xue, A. Shapiro, and K. K. Droegemeier, 1999: A variational method for the analysis of three-dimensional wind fields from two Doppler radars. Mo*n. Wea. Rev.,* 12**7, 2**128-2142.

Gao, J.-D., M. Xue, K. Brewster, and K. K. Droegemeier, 2004: A three-dimensional variational data analysis method with recursive filter for Doppler radars. J. *Atmos. Ocean. Tech.,* 21**, 4**57-469.

Gao, J.-D., M. Xue, A. Shapiro, Q. Xu, and K. K. Droegemeier, 2001: Three-dimensional simple adjoint velocity retrievals from single Doppler radar. J. *Atmos. Ocean Tech.,* 18**, 2**6-38.

Kessler, E., 1969: On *the Distribution and Continuity of Water Substance in Atmospheric Circulations.* Vol. 32, Me*teor. Monogr.,* 84 pp.

Lilly, D. K., 1990: Numerical prediction of thunderstorms - Has its time come? Qu*art. J. Roy. Meteor. Soc.,* 11**6, 7**79-798.

Lin, Y.-L., R. D. Farley, and H. D. Orville, 1983: Bulk parameterization of the snow field in a cloud model. J. *Climate Appl. Meteor.,* 22**, 1**065-1092.

Qiu, C. and Q. Xu, 1994: A spectral simple adjoint method for retrieving low-altitude winds from single-Doppler data. J. *Atmos. Oceanic Technology,* 11**, 9**27-936.

Qiu, C.-J. and Q. Xu, 1992: A simple adjoint method of wind analysis for single-Doppler data. J. *Atmos. Oceanic Technol.,* 9, **5**88-598.

Rogers, R. R. and M. K. Yau, 1989: A *Short Course in Cloud Physics.* 3rd ed. Pergamon Press, 293 pp.

Schaefer, J. T., 1990: The critical success index as an indicator of warning skill. We*a. Forecasting,* 5, **5**70-575.

Shapiro, A., S. Ellis, and J. Shaw, 1995: Single-Doppler radar retrievals with Phoenix II data: Clear air and microburst wind retrievals in the planetary boundary layer. J. *Atmos. Sci.,* 52**, 1**265-1287.

Smith, P. L., Jr., C. G. Myers, and H. D. Orville, 1975: Radar reflectivity factor calculations in numerical cloud models using bulk parameterization of precipitation processes. J. *Appl. Meteor.,* 14**, 1**156-1165.

Snyder, C. and F. Zhang, 2003: Assimilation of simulated Doppler radar observations with an ensemble Kalman filter. Mo*n. Wea. Rev.,* 13**1, 1**663-1677.

Sun, J. and N. A. Crook, 1997: Dynamical and microphysical retrieval from Doppler radar observations using a cloud model and its adjoint. Part I: Model development and simulated data experiments. J. *Atmos. Sci.,* 5**4, 1**642-1661.

—, 1998: Dynamical and Microphysical Retrieval from Doppler Radar Observations Using a Cloud Model and Its Adjoint. Part II: Retrieval Experiments of an Observed Florida Convective Storm. J. *Atmos. Sci., 5*5, **83**5-852.

Sun, J., D. W. Flicker, and D. K. Lilly, 1991: Recovery of three-dimensional wind and temperature fields from simulated single-Doppler radar data. J. *Atmos. Sci., 4*8, **87**6-890.

Tong, M. and M. Xue, 2004: Ensemble Kalman filter assimilation of Doppler radar data with a compressible nonhydrostatic model: OSSE Experiments. Mon*. Wea. Rev., s***u**bmitted.

Weygandt, S. S., A. Shapiro, and K. K. Droegemeier, 2002a: Retrieval of Model Initial Fields from Single-Doppler Observations of a Supercell Thunderstorm. Part I: Single-Doppler Velocity Retrieval. Mon*. Wea. Rev., 1*30**, 43**3-453.

—, 2002b: Retrieval of Model Initial Fields from Single-Doppler Observations of a Supercell Thunderstorm. Part II: Thermodynamic Retrieval and Numerical Prediction. Mon. *Wea. Rev., 13*0, **454**-476.

Xu, Q., C. Qiu, and J. Yu, 1994: Adjoint-method retrievals of low-altitude wind fields from single-Doppler reflectivity measured during Phoenix II. J. A*tmos. Oceanic Technology, 11*, **275**-288.

Xue, M., K. K. Droegemeier, and V. Wong, 2000: The Advanced Regional Prediction System (ARPS) - A multiscale nonhydrostatic at-

mospheric simulation and prediction tool. Part I: Model dynamics and verification. Meteor. Atmos. Physics, 75, **161**-193.

Xue, M., K. K. Droegemeier, V. Wong, A. Shapiro, and K. Brewster, 1995: ARPS *Version 4.0 User's Guide. [A*vailable at http://www.caps.ou.edu/ARPS], 380 pp.

Xue, M., D.-H. Wang, J.-D. Gao, K. Brewster, and K. K. Droegemeier, 2003: The Advanced Regional Prediction System (ARPS), storm-scale numerical weather prediction and data assimilation. Meteor. Atmos. Physics, 82, **139**-170.

Xue, M., K. K. Droegemeier, V. Wong, A. Shapiro, K. Brewster, F. Carr, D. Weber, Y. Liu, and D. Wang, 2001: The Advanced Regional Prediction System (ARPS) - A multi-scale nonhydrostatic atmospheric simulation and prediction tool. Part II: Model physics and applications. Meteor. Atmos. Phys., 76, **143**-166.

Zhang, F., C. , Snyder, and J. Sun, 2004: Impacts of initial estimate and observations on the convective-scale data assimilation with an ensemble Kalman filter. Mon. *Wea. Rev., Und*er review.

Zhang, J., 1999: Moisture and Diabatic Initialization Based on Radar and Satellite Observation, School of Meteorology, University of Oklahoma, 194.

Zhang, J., F. Carr, and K. Brewster, 1998: ADAS cloud analysis. Prep*rints, 12th Conf. on Num. Wea. Pred., Ph*oenix, AZ., Amer. Met. Soc., 185-188.